

Hybrid Electric Regional Turboprop Aircraft

A Technical Report submitted to the Department of Mechanical and Aerospace Engineering

Presented to the Faculty of the School of Engineering and Applied Science

University of Virginia • Charlottesville, Virginia

In Partial Fulfillment of the Requirements for the Degree

Bachelor of Science, School of Engineering

Catherine DeScisciolo

Spring, 2023

Technical Project Team Members

Vincent Fimiani

Kyle Hunter

Daniel Lattari

Kazi Nafis

Christian Prestegard

Michael Richwine







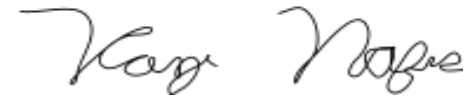


Robert Taylor

Nathan Vu

On my honor as a University Student, I have neither given nor received unauthorized aid on this assignment as defined by the Honor Guidelines for Thesis-Related Assignments

Jesse Quinlan, Department of Mechanical and Aerospace Engineering

Team E-Mission

Team Member	Role	AIAA #	Signature
Robert Taylor	Team Lead, Market and Mission Analysis	1403224	
Christian Prestegard	Co-Lead, Costing Analysis, Subsystem Design	1081593	
Catherine DeScisciolo	Aerodynamic Analysis, Control Surface Sizing	1423314	
Vincent Fimiani	Structure Design	1423294	
Kyle Hunter	Stability Analysis, Empennage Sizing	1423315	
Daniel Lattari	Aerodynamic Analysis, Wing Sizing	1143692	
Kazi Nafis	Landing Gear Design, Fuselage Configuration	1400154	
Michael Richwine	Propulsion Analysis, TMS Design	1371352	
Nathan Vu	Propulsion Analysis, EAP Design	1423060	
Jesse Quinlan	Faculty Advisor	-	

I. Executive Summary

Climate change has become an increasingly important issue in our daily lives. Commercial aviation is a significant contributor to global warming and air pollution, accounting for a significant proportion of annual global greenhouse gas emissions globally. However, as the world becomes increasingly connected, emerging economies in remote areas will need access to reliable, low-cost air routes in order to thrive. The Low Rider was designed to balance these competing needs by providing a sustainable way to connect regional markets across the world.

Wingtip mounted propulsors reduce drag, and are mildly hybridized on takeoff and climb. With a maximum range of 1000 nm, seating for 48 passengers, and short-field performance rivaling the best-in-class, the Low Rider is well-equipped to serve low-volume routes and remote markets. Relative to a baseline ATR 42-600 model, it is able to achieve a block fuel reduction of 33.4% on a 500 nautical mile economic mission, achieving a fuel burn of 0.077 lbs/seat-mile. In order to accommodate a wide variety of conditions, optional features include a gravel kit, for rough-field operations, and a supercooled large drop guard, for operations in extended icing conditions.

Table I.1 Low Rider Key Performance Parameters

Crew	2 flight crew, 1 attendant
Passenger Capacity	48
Cruise Speed (kts)	275
Cruise Altitude (ft)	30,000
Design Range (nm)	1,000
500 nm block fuel burn (lbs)	1,850
Takeoff Field Length (ft) MSL / 5000 ft	2870 / 3249
Landing Field Length (ft) MSL / 5000 ft	2608 / 2834
OEW (lbs)	20,961
MTOW(lbs)	37,255
Wingspan (ft)	91.8
Fuselage Length (ft)	75.5
Powerplant	2x 2900 SHP gas turbines, each connected with a 100 HP electric motor
Acquisition Cost (millions USD)	19.9
Direct Operating Cost (USD / hour)	8533.25

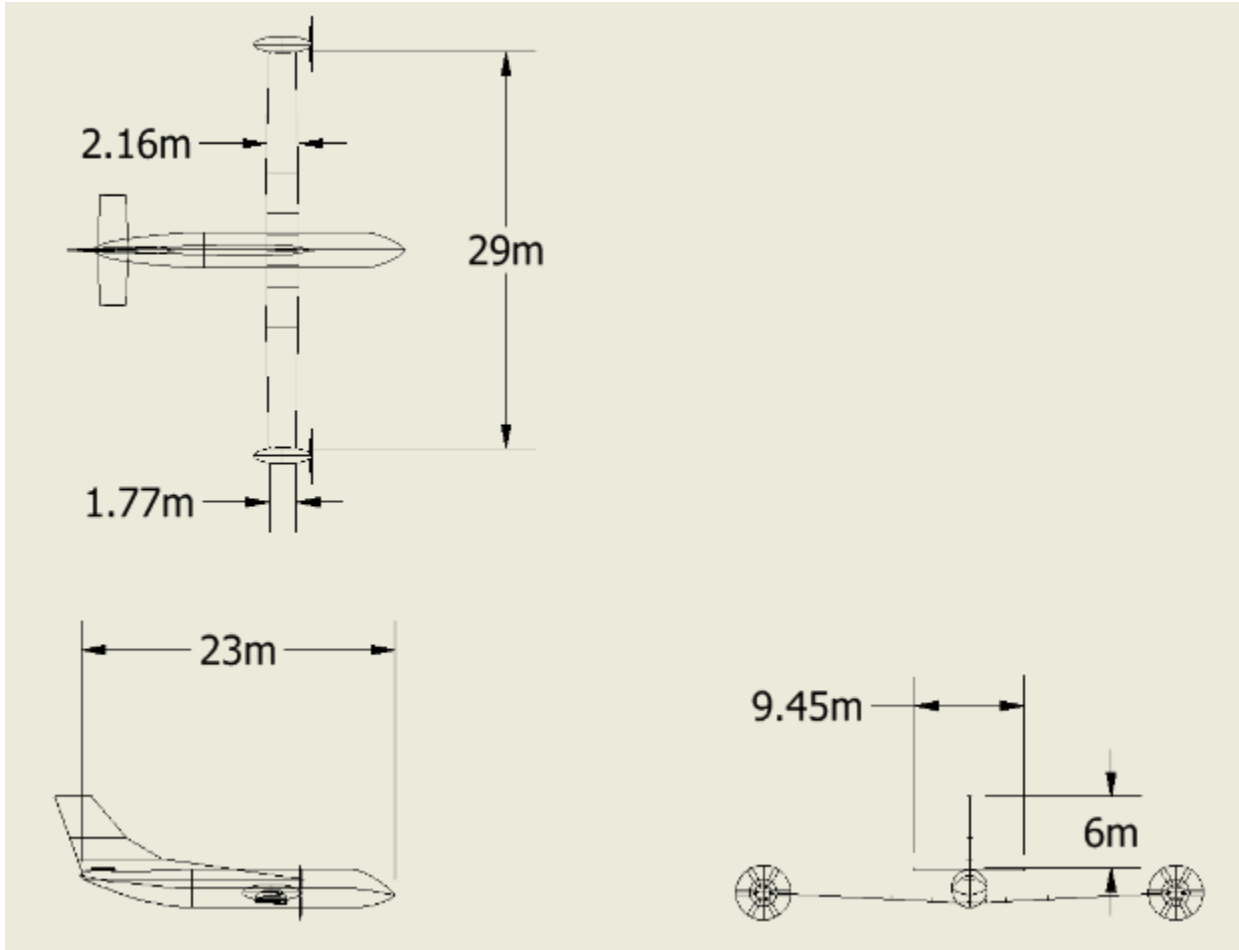


Figure I.1. Low Rider Dimensions

Contents

Team E-Mission	1
I. Executive Summary	2
Contents	4
II. List of Figures	6
III. List of Tables	7
IV. Symbols and Abbreviations	8
1. Introduction	8
1.1 Current Market and Competitors	8
1.2 Future Demand	11
1.3 Design Priorities	12
1.4 Performance Benchmark	13
2. Concept Ideation	14
2.1 Concept Design and Common Features	14
2.1.1 Concept 1: “Low Rider”	15
2.1.2 Concept 2: “TBW”	16
2.1.3 Concept 3: “DEP”	16
2.2 Concept Evaluation	17
2.2.1 Priority Weightings	18
2.2.2 Concept Selection	18
3. Mission Design	20
3.1 Mission Profile	20
3.2 Cruise Altitude Selection	21
3.3 Cruise Speed Selection	22
4. Initial Sizing and Constraints Analysis	23
4.1 MTOW Estimation	23
4.1.1 Procedure	23
4.1.2 Initial Sizing Estimation	24
4.2 Design Constraints	25
5. Aerodynamics	26
5.1 Wing Sizing	27
5.3 Airfoil Selection	29
5.5 High-Lift Devices	33
5.6 Wingtip Propulsor Benefit	35
6. Propulsion	36
6.1 Hybrid-Electric Architecture Comparison	36
6.2 Propulsion Architecture Comparison	37
6.3 Methodology, Calibration, and Reference Propulsion System	38
6.4: Gas Turboprop Engine	38
6.5 Electric Motor	42

6.6 Propeller Analysis	43
6.7 Energy Storage Selection	44
6.8 Battery Sizing Methodology	44
6.9 Hybridization Trade Study	46
6.10 Electrical System	47
6.11 Thermal Management System	49
6.12 Final Design Architecture and Claimed Benefits	50
6.13 Potential Future Technology	51
7. Structures	51
7.1 Fuselage Frame	51
7.2 Wing Box	52
7.3 Fuel Tanks	57
7.4 Landing Gear	58
7.4.1 Landing Gear Design	58
7.4.2 Gravel Kit	60
7.4.3 Main Gear	61
8. Weight and Balance	63
8.1 Final Weight Estimation	63
8.2 CG Location	65
9. Stability & Control	66
9.1 Empennage Design	66
9.2 Stability Analysis	67
9.3 Control Surface Sizing	69
9.4 OEI Considerations	69
10. Performance Analysis	70
10.1 Block Fuel Burn and Emissions	70
10.2 Flight Envelope	72
10.3 Performance Summary	74
11. Systems	76
11.1 Actively Tuned Vibration Absorbers (ATVAs)	76
11.2 Air Conditioning and Emergency Oxygen	77
11.3 Anti-Icing	78
11.4 Fire Suppression	78
11.5 Fly-By-Light / Power-By-Wire (FBL/PBW)	79
11.6 Full-Authority Digital Engine Control (FADEC)	80
11.7 Non-Propulsive Electrical System	80
12. Interior Layout	81
12.1 Fuselage Configuration	81
12.2 Passenger Cabin	82
12.3 Cockpit	84
12.3.1 Avionics	85

r12.3.2 Autonomous Operation	86
13. Maintenance	86
14. Cost Estimation	87
15. Conclusion	88
References	89

II. List of Figures

Figure 1.1: Distribution of Regional Aircraft Flight Distances
Figure 2.1: Shaded Model of Low Rider
Figure 2.2: Shaded Model of TBW
Figure 2.3: Shaded Model of DEP
Figure 3.1: Mission Profile
Figure 3.2: Difference in Block Fuel Burn for Various Cruise Altitudes Relative to FL280
Figure 3.3: Differences in Block Fuel Burn and Mission Time for Various Cruise Speeds Relative to 275 kts
Figure 4.1: Matching Plot of Mission Constraints, Highlighting the Target Design Region
Figure 5.1: Wingspan Trade Study
Figure 5.2: Coefficient of Lift vs Angle of Attack at Takeoff
Figure 5.3: Coefficient of Drag vs Angle of Attack at Takeoff
Figure 5.4: Lift over Drag vs Angle of Attack at Takeoff
Figure 5.5: Lift vs Drag at an Angle of Attack Ranging from -10° to 15°
Figure 5.6: Lift vs Drag during Cruise
Figure 5.7: Graph for Obtaining Preliminary Values for Flap Sizing
Figure 6.1: SFC Comparison between the Current Generation and the Next Generation Engines
Figure 6.2: NO_x Comparison between the Current Generation and the Next Generation Engines
Figure 6.3: Impact of Engine OPR on Total NO_x Emissions and Block Fuel Burn
Figure 6.4: XRotor Geometry Design Results
Figure 6.5: Generated Geometry Profiles
Figure 6.6: Impact of Battery Power Density and Hybridization Level on Battery Weight for Sufficient Battery Storage after Five Years
Figure 6.7: Fuel Burn Change Relative to the Next Generation Model at Different Levels of Hybridization
Figure 6.8: Energy Density at 1% Hybridization Effect on Battery Weight
Figure 7.6: Fuel Tank Parts Visual
Figure 7.8: Front Landing Gear without Gravel Kit
Figure 7.9: Front Landing Gear without Gravel Kit
Figure 7.10: Front Landing Gear with Gravel Kit
Figure 7.11: Front Landing Gear with Gravel Kit
Figure 7.12: Landing Gear Retraction
Figure 7.13: Landing Gear Retraction
Figure 7.14: Rear Landing Gear
Figure 7.15: Rear Landing Gear
Figure 8.1: Weight and Balance Diagram

Figure 9.1: Aerodynamic Forces vs Angle of Attack at Takeoff
Figure 9.2: Aerodynamic Moments vs Angle of Attack at Takeoff
Figure 10.1: Economic Mission Block Fuel Reduction Relative to ATR 42-600
Figure 10.2: Share of Block Fuel Reduction Relative to ATR 42-600 for Projected New Technologies
Figure 10.3: Gust Envelope
Figure 10.4: Maneuvering envelope
Figure 10.5: Payload-Range Diagram for Low Rider
Figure 11.1: Interior Subsystems
Figure 11.2: Configuration of ATVA Attached to Fuselage Structure
Figure 12.1: Fuel Burn per Seat-Mile • Operating Empty Weight vs Passenger Capacity
Figure 12.2: Top-Down View of Cabin Layout. Location of Passenger Entrances Indicated by the Black Arrow
Figure 12.3: Fuselage Centerline Diagram
Figure 12.4: Closeup View of Seats
Figure 12.5: Cross-Section of Fuselage
Figure 12.6: Interior of Saab 2000 Cockpit
Figure 12.7: Examples of SVS (left) and EFVS (right) Displays
Figure 14.1: Refueling Cost Comparison

III. List of Tables

Table 1.1: Summary of Comparable Aircraft
Table 1.2: Results of Benchmark Model Calibration
Table 2.1: Comparison of Key Metrics Concept Performance
Table 2.2: Comparison of Estimated Concept Costs
Table 2.3: Concept Evaluation Matrix
Table 4.1: Estimated Fuel Weight Fractions for each Mission Segment
Table 4.2: Component Weight Estimates
Table 5.1: Wing Geometry
Table 5.2: Parasitic Drag
Table 5.3: Empennage Sizing
Table 5.4: Changes in $C_{L,max}$ due to Flap Deflection
Table 6.1: Engine Characteristics Modeling Results
Table 6.2: Electrical Component Sizing Specifications
Table 7.1: Aluminium vs Carbon Fiber
Table 7.2: Fuel Tank Parts
Table 7.3: Landing Gear Parts
Table 7.4: Landing Gear Parts with Gravel Kit
Table 7.5: Rear Landing Gear Parts
Table 8.1: Component Weights and Approximate Locations
Table 9.1: Vertical Tail Sizing
Table 9.2: Horizontal Tail Sizing

Table 9.3: Aircraft Stability Coefficients

Table 10.1: Summary of Block Fuel Burn and Emission Reductions

Table 10.2: Key Aircraft Speeds

Table 10.3: Summary of Key Performance Metrics Relative to the ATR 42-600

Table 14.1: Costing Summary

IV. Symbols and Abbreviations

RT: Regional Turboprops

RJ: Regional Jets

SAR: Specific Air Range

SOA: State-of-the-Art

EIS: Entry Into Service

DEP: Distributed Electric Propulsion

TBW: Truss Braced Wing

SFC: Specific Fuel Consumption

TSFC: Thrust Specific Fuel Consumption

OML: Outer Mold Line

OEI: One Engine Inoperative

OPR: Overall Pressure Ratio

SAF: Sustainable Aviation Fuel

TEEM: Turbine Electrified Engine Management

HEMM: High Efficiency Megawatt Motor

TMS: Thermal Management System

COP: Coefficient of Performance

FEA: Finite Element Analysis

TOGW/MTOGW: (Maximum) Takeoff Gross Weight

GPS: Global Positioning System

IMU: Inertial Measurement Unit

1. Introduction

1.1 Current Market and Competitors

Due to their increased effective bypass ratio, turboprop engines have much lower specific fuel consumptions, and higher thrust-specific fuel consumptions (TSFC) at low speeds than jet engines. This means RTs are far more efficient than their RJ counterparts on short-haul routes, burning less fuel per seat-mile and having much higher specific air ranges (SAR) [1]. Consequently, they are significantly more profitable and produce fewer

emissions per seat-mile than their RJ equivalents [2]. They also require less runway than RJs. Current 50 pax turboprops need only about 4000 ft of runway to takeoff and land, while most 50 pax RJs require more than 5000 ft, some needing as many as 7800 ft. 24% of all RT flights are flown out of runways shorter than 6000 ft. [1], a distance which is inaccessible to many RJs. Table 1.1 below compares current aircraft in the 50-pax regional airliner market, including one RJ, the ERJ 145.

Greater efficiency and short-field performance means RTs are particularly well-suited to serving “origin-direct”, or O-D, markets. These are flights that serve “non-hub” or “secondary” airports, which generally have shorter runways and smaller customer bases. Direct flights on RTs complement existing infrastructure [2] and help overcome geographic barriers such as mountains or bodies of water.

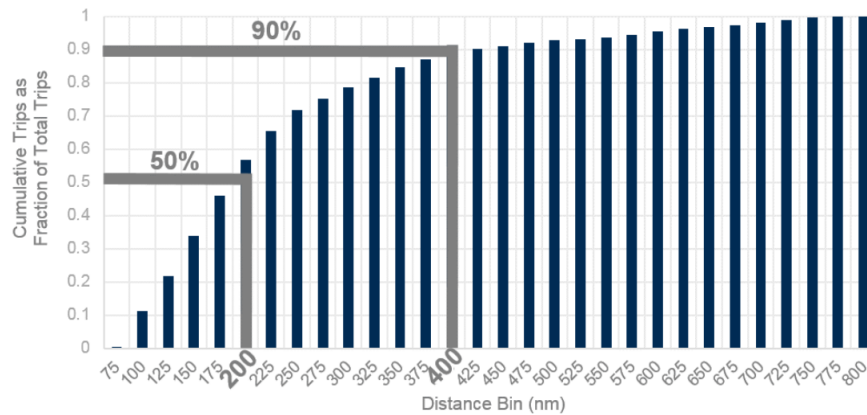


Figure 1.1: Distribution of Regional Aircraft Flight Distances

Globally, approximately 47% of all flights are less than 500 nm, and 90% of all regional flights are shorter than 400 nm [1]. Of the 3800 operating commercial airports in the world, 45% are served only by regional aircraft, and 34% are served exclusively by RTs [2]. Major RT operators, such as Air New Zealand or Japan Air Commuter, fly few or no routes longer than 400 nm. In the 41-60 pax RT category, the average flight distance is approximately 200-250 nm [1]. This makes performance on short missions a key driver of aircraft success in this class.

Table 1.1: Summary of Comparable Aircraft

	ATR 42-600¹	DHC-8 Q300²	Saab 2000³	ERJ 145⁴
Max. Passenger Capacity	48	56	58	50
Max. Range (nm)	726	924	1,549	1,550
Cruise Speed (kts)	289	287	370	460
Takeoff Field Length (ft)	3,632	3,864	4,005	7,448
Landing Field Length (ft)	3,196	3,415	4,005	4,593
Service Ceiling (ft)	19,685	25,000	31,000	37,000
Wingspan (ft / m)	81 / 24.6	90 / 27.4	81 / 24.7	66 / 20
Max. Payload (lbs)	11,574	11,389	12,125	12,775
OEW (lbs)	25,904	25 993	30 424	26,339
MTOW (lbs)	41,005	43,001	50,265	48,501
Years in Production	2007-Present	1998-2009	1992-1999	1992-2020
Number Delivered	1,600	267	63	742
Number of Operators	200	18	10	36
Unit Cost (millions USD)	19.5	18.6	15	19.6
Powerplant	PW127XT-M	PWC123	RR AE 2100P	RR AE3007
Manufacturer	Aero-Transport Regionale	DeHavilland Canada	Saab Aviation	Embraer

¹[3][4][5] ²[7][8] ³[9][10][11][12][13] ⁴[14][15][16][17]

Their operational flexibility also lends RTs to serving remote or underdeveloped regions and opening new routes. Latin America and the Caribbean, with its islands, sparsely populated areas, and lack of existing infrastructure, depend largely on RTs for domestic and intra-regional travel [ATR market analysis]. The strengths of RTs in remote regions are further highlighted in Alaska, which accounts for more than half of all O-D routes in the US [NASA/short haul]. RTs reduced operating costs and smaller capacity also provide airlines with a low-risk way to open new routes as they try to gauge and build demand. As these new routes mature, 35% of them will still operate RTs [ATR market analysis]. A successful RT must not only perform well on short missions, but also have the ability to reliably and economically serve remote areas.

1.2 Future Demand

With more than 100 routes projected to open annually [3] and almost 2500 turboprops expected to be delivered over the next 20 years [2], the next decade presents a tremendous opportunity to develop, produce, and deliver a new regional turboprop aircraft capable of meeting unique market needs. An entry year of 2035 will prove the opportunity to capitalize on the needs of the future economy.

A survey of 31 airlines conducted by Embry-Riddle Aeronautical University in 2013 indicates that the greatest demand for a new RT is in the 40-50 pax category. In this category, airlines believe that a maximum range of approximately 900 nm with a take-off distance of 4100 ft would be ideal [18]. This is in line with a market analysis run by NASA in 2018, which determined that a 48-passenger hybridized RT with a range of 600 nm would be best equipped to serve short-haul markets. As RTs generally serve low-volume routes with longer turnaround times [1], battery charging times are not expected to limit aircraft electrification. As such, the RTs present an ideal space to test out and develop novel hybrid-electric propulsion architectures.

1.3 Design Priorities

In order to be a competitive option for regional airlines, the aircraft must meet and exceed the capabilities of current competitors. Increased profitability would incentivize airlines to establish new routes in US domestic markets, and promote growth and access abroad. Reducing block fuel burn by 20% or more with EAP will not only have a major impact on aircraft emissions, but also significantly reduce operating costs and incentivize new routes. As the vast majority of RT flights are shorter missions, the design will target efficiency on a longer-distance representative economic mission of 500 nm. A “greener” aircraft will also make this aircraft more marketable in the face of changing consumer attitudes and increased regulatory pressure.

The projected growth in emerging economies means this aircraft has the opportunity to more sustainably connect new parts of the world to global markets. The ability to take off and land on short runways with variable conditions will maximize the number of available airports. Shorter runways are less expensive to build and operate, so increased performance will also help lower barriers to opening new routes. To operate in less developed regions, the aircraft must require minimal support infrastructure, and be able to survive punishing environments. An aircraft

that is easily repaired and maintained will be better able to serve these regions, and has the added benefit of reduced costs on the airline.

In order to gain widespread acceptance, the aircraft must be attractive to purchase by the airlines. A simpler, more easily manufactured aircraft will have a far more competitive price tag and can be produced in sufficient numbers to meet projected demand. New technologies are more expensive up-front, but a more expensive unit cost is acceptable to airlines if the lifetime cost is lower [18]. Increased efficiency and minimal required maintenance will help to significantly reduce lifetime operating costs and offset the acquisition cost.

Propeller-driven aircraft are perceived as outdated and less safe by the public, due partially to their increased cabin noise and the outward appearance. A modern-looking RT designed with comfort in mind will improve customer acceptance of an aircraft with many clear commercial and environmental advantages on short-haul routes [19]. In the face of volatile fuel prices, increased fuel efficiency will help ticket prices low, making the RT an even more attractive option for both airlines and their passengers.

With future market needs in mind, key design priorities were laid out as follows:

1. **Environmental Footprint:** Exceed benchmark aircraft capabilities and environmental impact
2. **Performance:** Can operate in small airports, harsh climates, and adverse weather conditions
3. **Reliability and Maintainability:** Durable, resilient systems that are easy to maintain
4. **Cost:** Inexpensive to manufacture, purchase, and operate
5. **Appearance and Comfort:** Interior and exterior aesthetics easily accepted by customers

1.4 Performance Benchmark

The ATR 42-600 is the youngest aircraft in the RT market (Table 1.1) and ATR's 42 series is the most popular aircraft in the 50-pax category, with more operators and deliveries than any other RT in service. The 42-600 was thus considered to be the SOA, and a calibrated FLOPS model was used as the benchmark against which our aircraft performance would be measured.

Block fuel is the primary metric of this design challenge, so the FLOPS model was modified to match for the fuel burns given by ATR. Block fuel burn for a 500 nm mission is not provided by ATR, however it does provide numbers for 200, 300, and 400 nm. Using known weights, dimensions, and mission parameters of the ATR 42-600, the model was calibrated to match each of these fuel burns to within 5% error, minimizing the error from the published 400 nm mission. This calibrated model was then used to predict the BFB of our benchmark on a 500 nm mission, as seen in Table 1.2.

Table 1.2 Results of Benchmark Model Calibration

Mission Distance (nm)	Fuel Burn (lbs)		% Difference
	Calculated	ATR Values	
200	1208.8	1272	-4.97
300	1724.3	1733	-0.5
400	2247.3	2247	0.01
500	2776.1	-	-

2. Concept Ideation

2.1 Concept Design and Common Features

The ATR 42-600, Dash 8-Q300, and Saab 2000 are well-established aircraft in the RT market. Because of their popularity and market dominance, all three concepts draw inspiration from these designs. However, a variety of substantially different advanced configurations were considered within this framework to ensure a large area within the design space was considered.

Some standardized features were decided on in the conceptual design phase in order to provide an objective perspective on the benefits and penalties of each concept and minimize the time required to close the designs:

- 1) The ATR 42-600 holds 48 passengers in a 2-2 fuselage layout. As this is assumed to be both the SOA and benchmark, all three concepts share the same passenger capacity, cabin layout, and fuselage dimensions.
- 2) In order to account for the effect of hybridization on these concepts, they were all assumed to draw 15% of their energy from an onboard Li-Ion battery on takeoff and climb. The batteries were sized using the same

methodology, and projected lifetime was not accounted for. A realistic energy density projection of 500 Wh/kg [27] was used in the battery sizing routine.

The validity of these assumptions was investigated following concept selection and refinement.

Each concept's geometry was modeled in NASA's Vehicle Sketch Pad (OpenVSP), a 3D modeling software designed for conceptual aircraft design. Various aircraft components, such as the fuselage, wing, or engine nacelles, can be dimensioned and placed to form a rough model of the concept's outer mold line (OML).

2.1.1 Concept 1: "Low Rider"

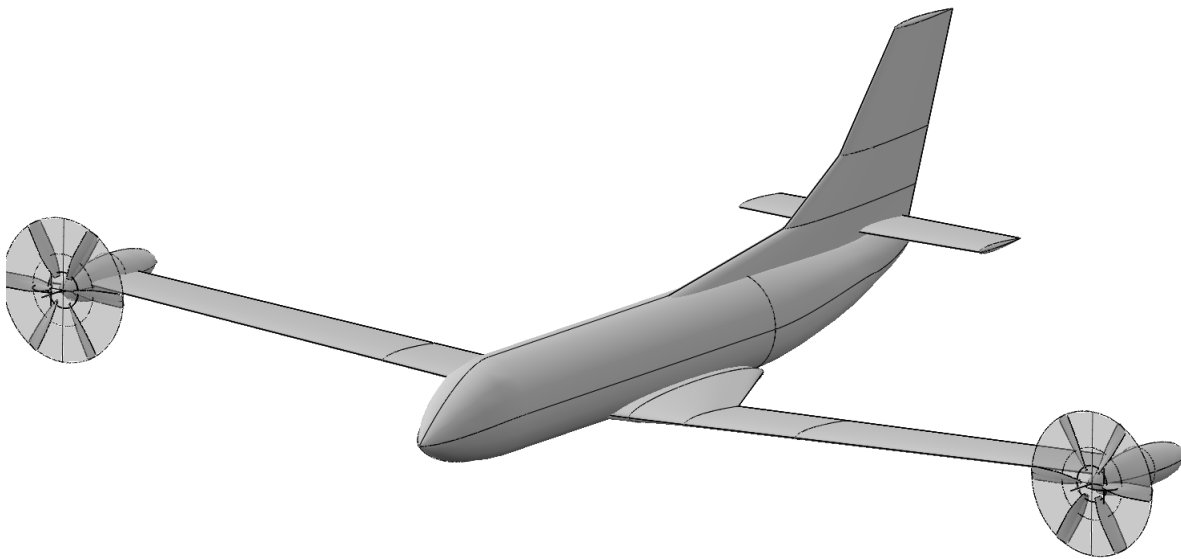


Figure 2.1. Shaded Model of Low Rider

Low Rider is a low-wing aircraft inspired by the Saab 2000. Its counter-rotating wingtip-mounted propellers significantly reduce the induced drag of the wings [nasa pegasus], while their increased distance from the fuselage decreases cabin noise. The propellers are powered by turboprops hybridized in parallel, drawing energy from the battery on takeoff and climb in order to reduce the turbine power requirements. To account for the substantial yaw under OEI conditions, the vertical tail is drastically larger in size. The low-wing configuration includes a large root to provide extra volume for batteries and landing gear in an aerodynamically efficient lifting-body shape. By placing the landing gear on the same spar as the wing, structural weight can be reduced.

2.1.2 Concept 2: “TBW”

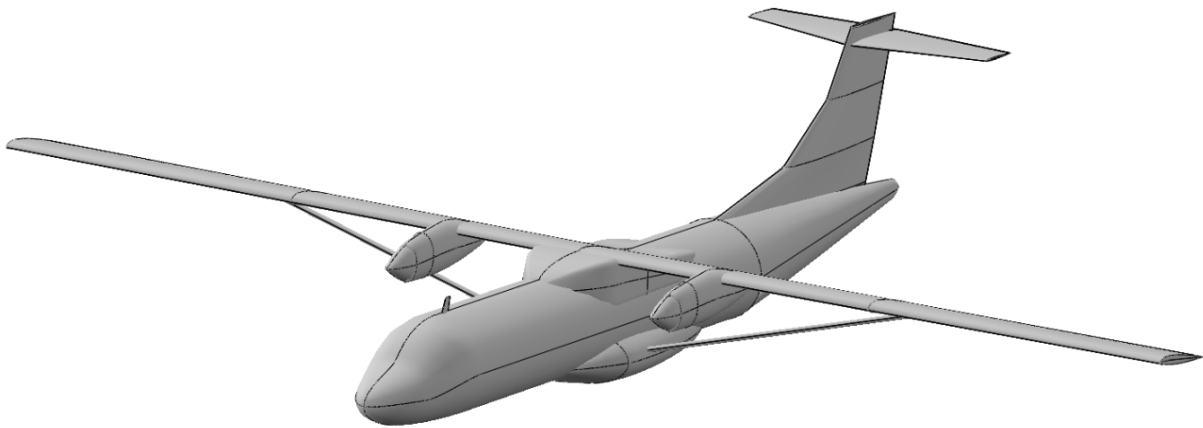


Figure 2.2. Shaded Model of TBW

TBW takes advantage of wing struts to drastically increase its wingspan. Modeled on the ATR 42-600, the larger aspect ratio greatly decreases its induced drag, allowing for a more efficient wing during both takeoff and cruise. The struts are shaped to provide lift and reduce form drag. In order to keep the truss in compression, the wing is mounted above the fuselage. A high-cruciform tail keeps the elevator out of the wash from both the propellers and struts, increasing its efficiency and reducing its size. The parallel-hybrid engines are located inboard in order to save on structural weight. The fuselage blisters provide extra volume for batteries and landing gear while supporting the struts.

2.1.3 Concept 3: “DEP”

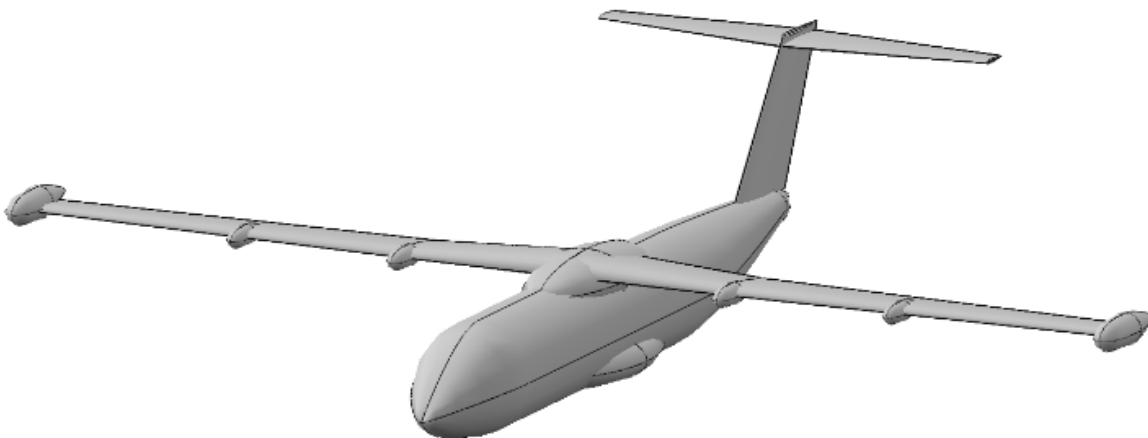


Figure 2.3. Shaded Model of DEP

DEP, like TBW, bases its structure and layout on the ATR 42-600. This concept takes advantage of distributed electric propulsion to increase the lift per unit span of the wing on takeoff and climb, allowing the wing to be sized for cruise and descent. A high-mounted wing increases propeller clearance, while a high-cruciform empennage keeps the elevator out of propeller and wing wash. Most of the thrust is provided by wingtip-mounted turboprops hybridized in parallel to reduce drag and increase aerodynamic efficiency. The inboard propulsors are fully electric and operate on battery power. They provide additional thrust during takeoff and climb, but are inoperative during cruise to save battery weight. However if one of the turboprops fails they can be restarted to help control yaw. The propellers fold in during cruise to reduce parasitic drag. Fuselage blisters provide extra volume for batteries and landing gear.

2.2 Concept Evaluation

Airfoil selection, wing and empennage sizing, and propulsion architecture models were completed for each concept prior to selecting the preferred concept. At this stage of the process, the design and evaluation philosophy was one of “precise inaccuracy”. Basic assumptions and rough, unrefined models were used, with the goal of simply being consistent in their application. This was done to level the playing field and make sure that each concept was evaluated fairly against the others.

Mission analysis was performed in NASA’s Flight Optimization Software (FLOPS). Using basic aircraft parameters such as geometry, passenger capacity, engine data, and mission profile, an aircraft’s performance on specified missions can be evaluated. This is done by first estimating aircraft aerodynamics and component weights from statistical and empirical models developed from existing aircraft, scaling the engine to meet mission requirements, optimizing the mission profile, and then “flying” this aircraft on the optimized mission to determine its performance [20].

The costing analysis was done in the Advanced Aircraft Analysis (AAA) 5.0 program. AAA takes weights and other mission- and sizing-related values as inputs and uses them along with prescribed parameters to produce outputs related to costs of the aircraft over its lifespan.

2.2.1 Priority Weightings

Once the concepts had been modeled to the same level of fidelity, they were evaluated according to our five design priorities. Each priority was weighted according to their importance, and the concepts were scored on a scale of one to five. This scale captures both the relative performance of each concept and their absolute performance to the benchmarks.

Reducing the environmental impact of our aircraft is the primary goal of our design and the key metric of performance given in the RFP. As such, it was given the greatest weighting.

Performance determines the number of airports the aircraft can access, as well as the weather conditions in which it can operate. A major goal of our final design is to build an aircraft capable of operating in as many places as possible, which includes short runways and a wide variety of temperatures. Reliability and maintainability drive how attractive the aircraft will be from an logistical perspective, and will also be a deciding factor in how far the aircraft can operate from major hubs. Both of these priorities were thus given an equal weighting.

As a result of their additional complexity and usage of batteries, hybrid-electric aircraft will by necessity have a greater up-front cost. Additionally, this aircraft will require retraining of both flight and maintenance crews, thus incurring additional operational costs over its lifetime. Given the reality of expensive new technologies, it was believed that cost must not be as great a concern in the evaluation process.

Customer acceptance will play a role in aircraft marketability, and this has always been an issue for RT aircraft. If this aircraft is to make a significant impact on regional aviation emissions, it must be bought by airlines and used regularly. A modern-looking airliner with a comfortable, quiet interior will be far more attractive to customers, and thus airlines.

2.2.2 Concept Selection

Once preliminary sizing and mission analysis on each of the three concepts had been completed, their performances were evaluated based on the weightings of our five design priorities. The results of the concept mission and costing analyses can be found below:

Table 2.1 Comparison of Key Metrics Concept Performance

Aircraft	Economic Mission		Field Length (ft)	
	Block Fuel Burn (lbs)	% Difference from SOA	Takeoff	Landing
ATR 42-600	2776	-	3632	3412
Low Rider	2007	-27.68	2845	4163
TBW	2007	-26.91	3427	4694
DEP	2029	-27.71	3594	4817

Table 2.2 Comparison of Estimated Concept Costs

Aircraft	Cost for 500 Aircraft (Billions USD)				DOC (USD/hour)
	R&D	Acquisition	Operation	Lifetime	
Low Rider	0.36	25.4	215.6	268.3	5891
TBW	0.36	25.6	675.5	779.4	8479
DEP	0.37	34.6	784.2	910.2	9909

All three concepts were able to achieve significantly reduced block fuel burns, with Low Rider and TBW providing an almost identical benefit. However, Low Rider demonstrated significantly improved takeoff performance from the ATR 42-600, while also having the greatest landing performance of the three concepts. Our costing estimates, although rudimentary, show that Low Rider holds a clear advantage in operating cost, and marginal advantage in acquisition cost. As these concepts all contain untested technologies with uncertain costs, however, the highest possible score given was three.

Reliability, maintainability, appearance, and comfort were all evaluated qualitatively. All concepts contain new technologies and materials that will have a learning curve in terms of reliability and maintenance, but Low Rider has the simplest airframe and most accessible wing. TBW's truss will complicate maintenance on the engine, and may experience unpredictable loads due to its unproven technology. DEP carries several more motors that can fail and must be maintained than the other concepts, and the folding inboard propellers will present an additional point of failure that will be difficult to maintain.

Appearance and comfort are inherently subjective. A group of 20 non-engineering students was polled in order to get an unbiased opinion on appearance more representative of the general populace. The average of each

concept’s ranking from this pool, rounded to the nearest integer, was then used to score each concept. It was assumed that each aircraft could have an equally comfortable and quiet interior.

Table 2.3 Concept Evaluation Matrix

Design Priority	Weighting	Low Rider	TBW	DEP
Environmental Impact	5	5	5	4
Performance	4	5	4	3
Reliability + Maintainability	4	3	2	2
Cost	3	3	2	1
Appearance + Comfort	2	4	3	3
Total Score	90	74	69	47

With clear advantages across the board, Low Rider was selected as the preferred concept for further development.

3. Mission Design

3.1 Mission Profile

Foremost among the shortcomings of planned hybrid-electric competitors is their limited range. The Heart Aerospace ES-30, a hybridized RT with a planned 2028 EIS, has a maximum range of approximately 430 nm with only 25 passengers [21]. A design range of 1000 nm allows Low Rider to cover over 95% of all routes served by RJs [1] and exceed the maximum range of competitor RTs. This provides increased flexibility and broader airline appeal,

especially if the aircraft is to help replace RJ service.

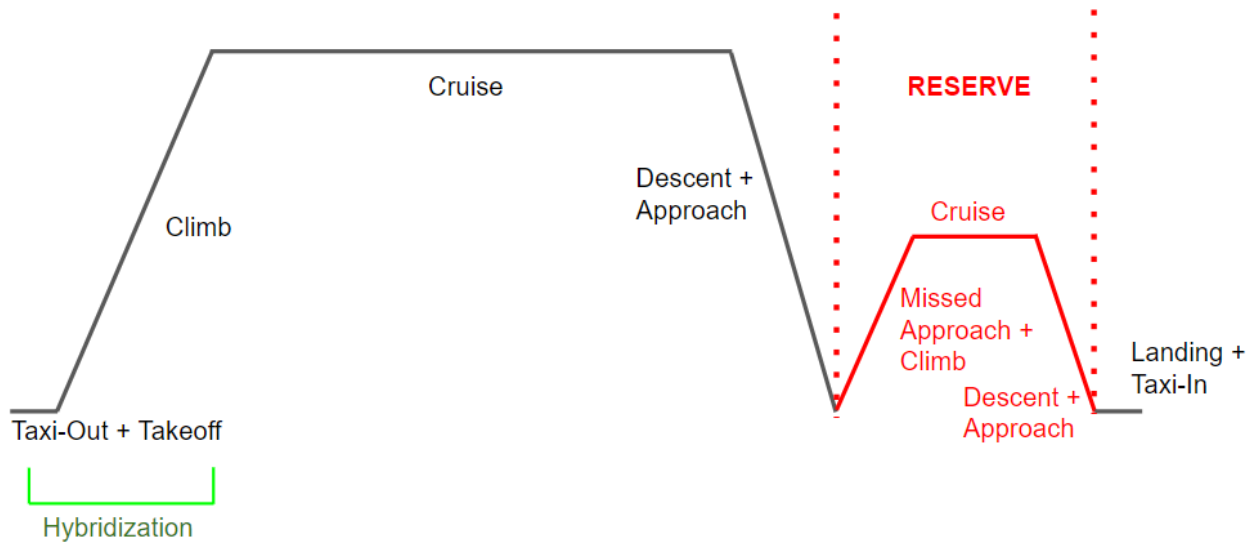


Figure 3.1. Mission Profile

Hybridization has the potential to greatly improve block fuel burn. However, the low energy density of conventional batteries makes them unsuitable for providing large amounts of energy. In order to maximize the benefits of electrification, Low Rider is only hybridized on takeoff and climb. Aircraft engines must be oversized to provide sufficient thrust for this fairly short mission segment. By using battery-powered electric motors to assist here, engine weight can be reduced and battery size can be kept to minimum.

Low Rider is designed for optimal L/D at cruise. In order to maximize time at this optimum, the cruise segment is flown at constant altitude and speed. As a transport-class aircraft, Low Rider is subject to FAR Part 25, which requires it to carry enough fuel for a reserve mission to an alternate airport following the design mission. Following ATR's assumptions and Federal regulations for nighttime IFR, the reserve mission includes a missed approach and climb, an alternate airport distance of 87 nm, followed by 45 min holding pattern, a final approach, and an extra 3% fuel allowance [1] [22].

r3.2 Cruise Altitude Selection

Cruise altitude can have a major impact on total fuel burn and overall mission performance. In order to determine the optimal altitude which would minimize fuel burn, seven altitudes ranging from 26,000 ft to 36,000 ft

were examined. The RFP specifies a minimum cruising altitude of 28,000 ft, however 26,000 ft was included in this study to ensure a minimum point did not lie below this limit. A slightly larger powerplant than the PW127 was modeled in order to provide sufficient power to climb, but an increase in SHP from 2750 to 3000 was found to actually reduce overall fuel burn. FLOPS was used to size a series of variations of the Low Rider model for each of these points, and their performance on a 500 nm economic mission, flying at a cruise speed of 275 kts was then estimated. The results were evaluated relative to the 28,000 ft case analyzed during concept selection. As seen in Figure 3.2, a minimum block fuel burn can be achieved by cruising at FL300. It was thus decided to fly Low Rider at a 30,000 ft cruise altitude.

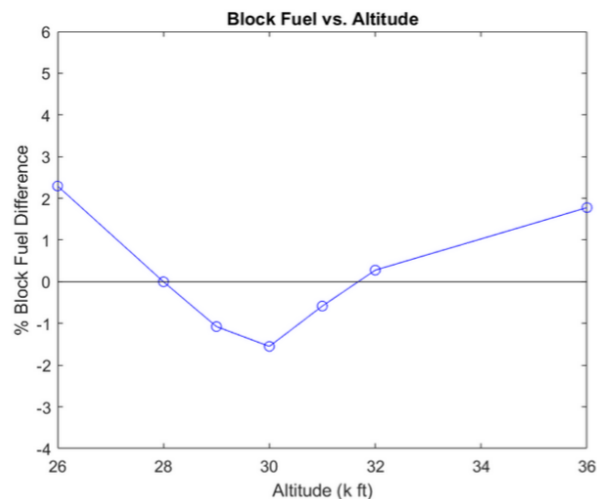


Figure 3.2. Difference in Block Fuel Burn for Various Cruise Altitudes Relative to FL280

r3.3 Cruise Speed Selection

Following altitude selection, cruise speed was next examined. Cruise speed drives total mission time and a shorter flight time can help improve customer acceptance, at the cost of increased block fuel burn. In order to understand the trade between block fuel burn and mission, four speeds ranging from 260 kts to 320 kts were examined. Using the same methodology found in Section 3.2, FLOPS was used to size and analyze aircraft performance on the 500 nm mission at FL300. The results of this study are shown in Figure 3.3, where performance is evaluated relative to the 275 kts case.

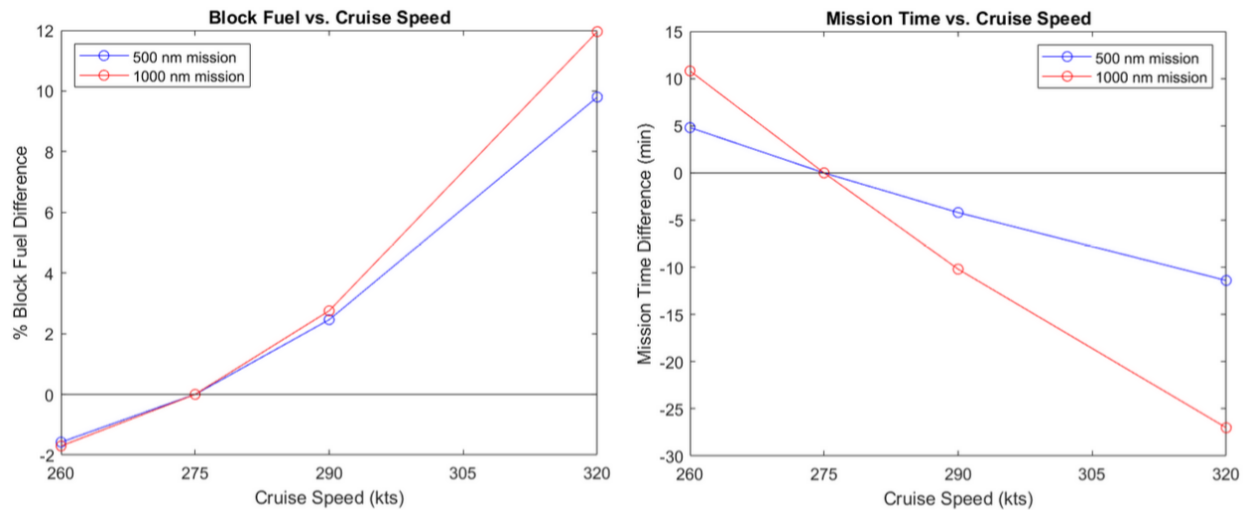


Figure 3.3: Differences in Block Fuel Burn and Mission Time for Various Cruise Speeds Relative to 275 kts

As expected, total fuel consumption rises dramatically with an increased cruise speed, while mission time is only reduced by a few minutes. On a 500 nm mission, cruising at 320 kts would burn almost 10% more fuel, while only reducing travel time by just over ten minutes. On even shorter missions, which market analysis indicates are far more common, this trade would be even more stark. As mitigating environmental impact is our highest priority, and ten minutes is a negligible amount of extra time for a customer to travel, it was decided to fly Low Rider at the RFP minimum cruising speed of 275 kts.

4. Initial Sizing and Constraints Analysis

r4.1 MTOW Estimation

4.1.1 Procedure

Initial sizing was performed using the method outlined in Chapter 5 of Carichner & Nicolai. Per RFP specifications, the fixed weight of crew, passengers, and baggage for a 48-passenger aircraft was determined to be 12,180 lb [23]. The battery weight was estimated by assuming 15% of the energy from the takeoff and climb segment fuel burns were provided by stored electrical energy. Then total fuel burn was calculated to be 85% percent of total fuel burn calculation to account for this hybridization. These assumptions were later found to be incorrect,

and the final battery sizing methodology can be found in Section 6. Statistical equations in Nicolai and Carichner were then used to estimate W_e/W_0 as 0.51 and $(L/D)_{max}$ as 19. Engine SFC was estimated from engine data for the current generation PW127 baseline engine [24]. Taxi, takeoff, and descent and landing fuel fractions were estimated from Carichner & Nicolai, while the cruise fuel fraction was calculated from rearranging the Breguet Range Equation (Eq. 4.1) into Eq. 4.2.

$$R = \frac{V}{SFC} (L/D)_{max} \ln\left(\frac{W_i}{W_{i+1}}\right) \quad (4.1)$$

$$\frac{W_{i+1}}{W_i} = \exp\left(-\frac{R \cdot SFC}{V_{cruise} (L/D)_{max}}\right) \quad (4.2)$$

Consistent with the Part 25 requirements laid out in Section 3.1, the reserve mission fuel fractions were calculated using the same methodology, where the missed approach and climb is considered to be the same as another takeoff segment.

4.1.2 Initial Sizing Estimation

Using the methods above and the mission profile defined in Section 3.1, the final mission weight fractions were calculated, and can be found in Table 4.1.

Table 4.1. Estimated Fuel Weight Fractions for each Mission Segment

	Segment	Fuel Fraction
Design Mission	Taxi + Takeoff	0.97
	Climb	1.00
	Cruise	0.94
	Landing	0.97
Reserve Mission	Takeoff	0.97
	Climb	1.00
	Cruise	0.98
	Landing	0.97
Final	Mission Weight Fraction	0.82

	Mission Fuel Fraction	0.18
--	-----------------------	------

Based on these weight fractions, Low Rider's initial MTOW estimate was 53,547 lbs. A complete list of initial weight estimates is included in Table 4.2 below. These values were used to guide preliminary design work and determine the initial constraints found in Section 4.2.

Table 4.2. Component Weight Estimates

Component	Estimate (lbs)
Battery	4,936
Fixed (incl. Battery)	17,566
Fuel	8,599
Empty	27,383
MTOW	53,547

r4.2 Design Constraints

In order to give an idea of how large the wing and how powerful the engine must be, the mission constraints must be used as bounds on the design space. FAR Part 25 requires two-engine aircraft be able to achieve an initial climb gradient of 2.1% [22]. The cruise speed (275 kts) was determined in Section 3.3, while the maximum approach speed (140 kts) and takeoff/landing field lengths (4500 ft) are specified by the RFP in order to allow operations on shorter fields. Section 3.2 determined the optimal cruising altitude to be 30,000 ft. In order to minimize the power required, this was also made the cruise ceiling, defined in NASA studies as the highest altitude where a climb rate of 300 ft/min can be achieved [NASA/ pegasus]. The equations found in Chapters 5 and 17 of Raymer were used to plot these mission constraints as functions of thrust and wing loading in Figure 4.1.

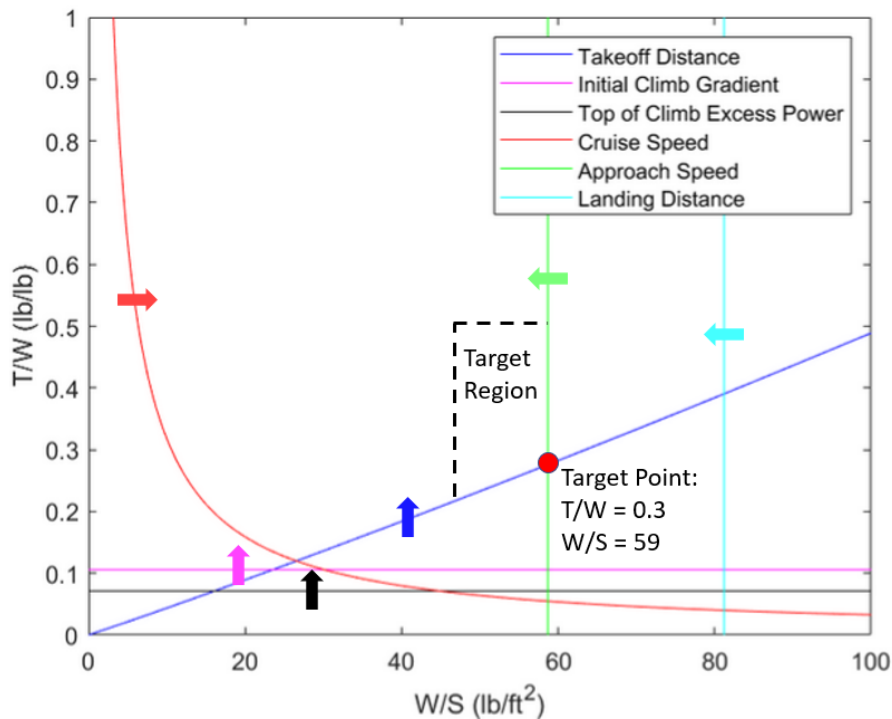


Figure 4.1: Matching Plot of Mission Constraints highlighting the Target Design Region

With an initial weight determined, wing and thrust rating can be estimated. It was decided to target the region with the lowest thrust loading and highest wing loading. A lower thrust loading means a lighter, cheaper engine can be used. The highest possible wing loading was targeted to reduce wing weight and cost, and improve ride comfort for the passengers. For an estimated MTOW of 53,547 lbs, the target point corresponds to a wing area of 906 ft² and a thrust rating of 16,064 lb, or approximately 8,000 lb per engine.

5. Aerodynamics

Aerodynamics studies were done to determine the optimal wing, empennage, and control surface sizes. These studies were cross-disciplinary, with the goal of providing valuable flight and aircraft information to corresponding teams.

The first step was to identify the airfoil requirements. These came from referencing both the RFP and the design priorities set out by the team. With the requirements defined, testing began on differing NACA airfoils and

their benefits, as well as varying these airfoils' dihedral angles and sections. With an airfoil selected, the team conducted studies to determine the precise wing size needed to achieve optimal aerodynamic performance. This same testing was then performed for the empennage. Utilizing all this information, a trade study was then performed to down-select wing sizes and create an envelope which reconciled aerodynamic performance with required block fuel. Finally, wing rework and sizing was completed to finalize aerodynamic data and then cross-disciplinary work was conducted to incorporate desired subsystems and high-lift devices.

Aerodynamic analysis was performed using the VSPaero and Flight Stream aerodynamic modeling software. VSPaero is a powerful aerodynamics simulation software tool that uses a vortex-lattice method to simulate the aerodynamic forces acting on an aircraft. In this analysis, VSPaero was used to predict the lift, drag, and other aerodynamic forces that would act on the aircraft model at different angles of attack. By studying the effects of changing design parameters such as wing shape and size, VSPaero allowed for an in-depth analysis of the aerodynamics of the model. VSPaero also provides a tool for creating and determining how high lift devices such as ailerons and flaps will contribute to the aerodynamic performance of the aircraft. In this analysis, Flight Stream was used to simulate the takeoff and climb performance of the aircraft, studying its performance at different angles of attack for takeoff and climb. This tool was used to analyze dynamic aspects of takeoff, climb, and cruise, helping to determine an envelope in which the aircraft performs best.

5.1 Wing Sizing

A crucial utility of these applications was to determine the most efficient airfoil type and size given the team's objectives. To do so, many iterations of the aircraft were created and run through both softwares to determine span, chord, dihedral angles, and other airfoil characteristics that provided the best performance. Through many such tests, the NACA 6612 airfoil was determined to be the best for the purposes of this aircraft and the objectives laid out by the RFP and the team's hierarchy of design priorities.

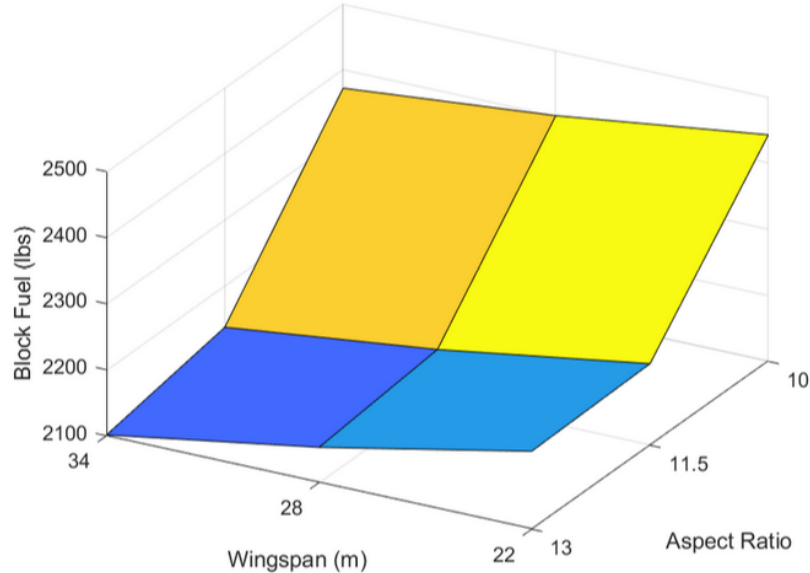


Figure 5.1: Wingspan Trade Study

Through auxiliary models in FLOPS, the figures above and below were produced to visualize the effects of aspect ratio and wingspan on block fuel burn. This model, in conjunction with the aerodynamic characteristics proven over a multitude of iterations, helped determine the desired aspect ratio and wingspan.

With this information, many design iterations were able to be dismissed and a specific design envelope was developed to connect this study, the aforementioned matching plot, and the aerodynamic performance displayed by individual models. This envelope stressed the importance of an aspect ratio in the range of 12-13 and a wingspan of 28-32 meters. Based on Figure 5.1, block fuel burn is more sensitive to changes in aspect ratio than span, so a span on the lower end of the optimal range indicated in the trade study was chosen in order to increase the wing loading. A higher wing loading makes for a more comfortable ride for passengers and passengers' safety and comfort in a turboprop is an important consideration for the design.

Using FLOPS weight estimations, Low Rider's MTOW was estimated as approximately 37,255 lbs. For a target W/S of 59 (Figure 5.1), this corresponds to a wing area of 641 ft². The wing also needed to be able to contain other aircraft systems such as the landing gear. As such, cross-disciplinary studies needed to be conducted to determine a feasible design for both the wing and its subsidiary components. From here the final design of the wing could be clarified based on design priorities. The final wing geometry can be found in Table 5.1 below.

Table 5.1: Wing Geometry

Parameter	Value
Span (ft)	91.8
Area (ft ²)	641
Aspect Ratio	13
Root Chord (ft)	7.1
Tip Chord (ft)	5.8
Mean Aerodynamic Chord (ft)	2.1
Taper Ratio	0.83
Dihedral (deg.)	3

Although this span exceeds the RFP ideal target of 24 m or 78.7 ft, no current competitor aircraft achieves this target. Low Rider's target market is smaller airports, and while it may be too large for an ICAO Code B gate, these airports are assumed to have sufficient space to simply allow passengers to board from the tarmac, removing the need for a gate entirely.

5.3 Airfoil Selection

The airfoil selected for this design is the NACA 6612. It has a maximum camber of 6% located 60% from the leading edge and a maximum thickness of 12% of the chord. This geometry was selected to achieve a high maximum C_L and reduce viscous drag due to its high camber and large leading edge radius. This also eliminated the need for leading edge flaps. An angle of attack of 9° at a speed of 191.52 ft/s are the takeoff conditions for this aircraft. In those conditions, the aircraft has a coefficient of lift of 1.57 without high lift devices and a coefficient of drag of 0.203 as can be seen in Figure 5.2. The highest lift-to-drag ratio is at an angle of attack of 2° , meaning the aircraft is optimized for cruise conditions.

Coefficient of Lift vs. Alpha (M=0.17, Sea Level)

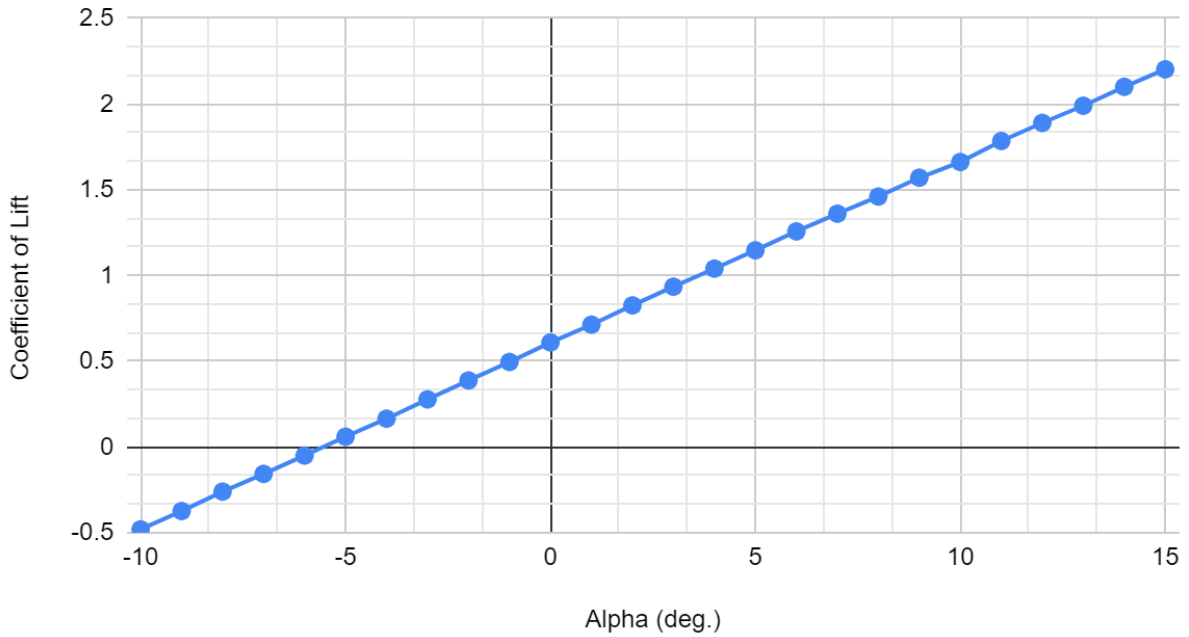


Figure 5.2: Coefficient of Lift vs Angle of Attack at Takeoff

Coefficient of Drag vs. Alpha (M=0.17, Sea Level)

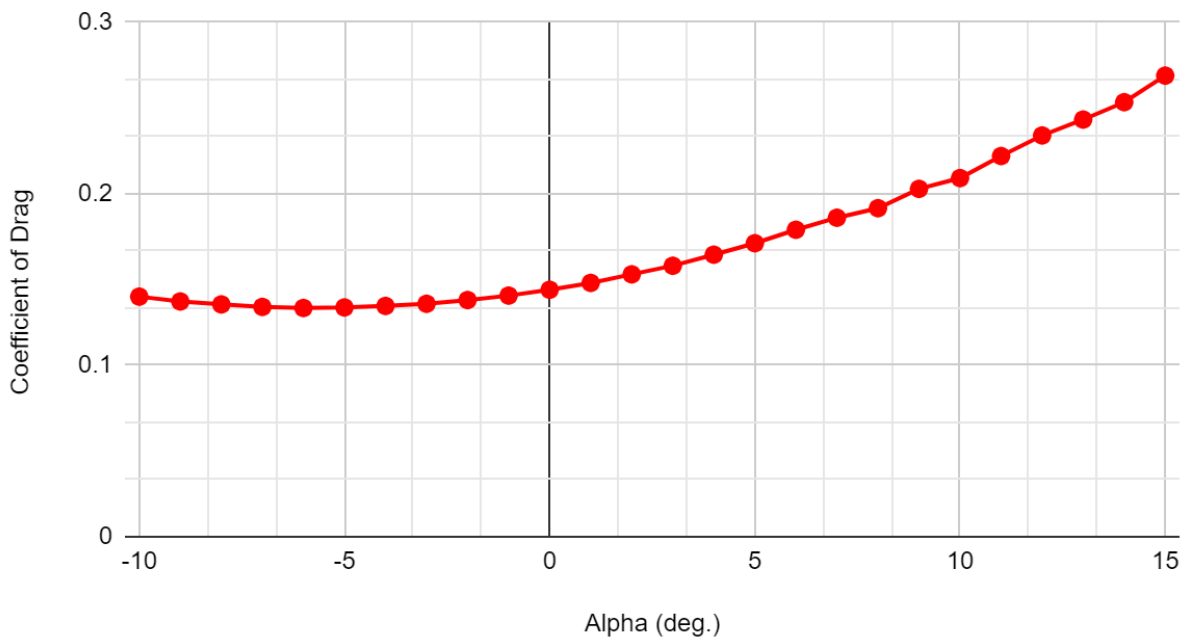


Figure 5.3: Coefficient of Drag vs Angle of Attack at Takeoff

L/D vs. Alpha

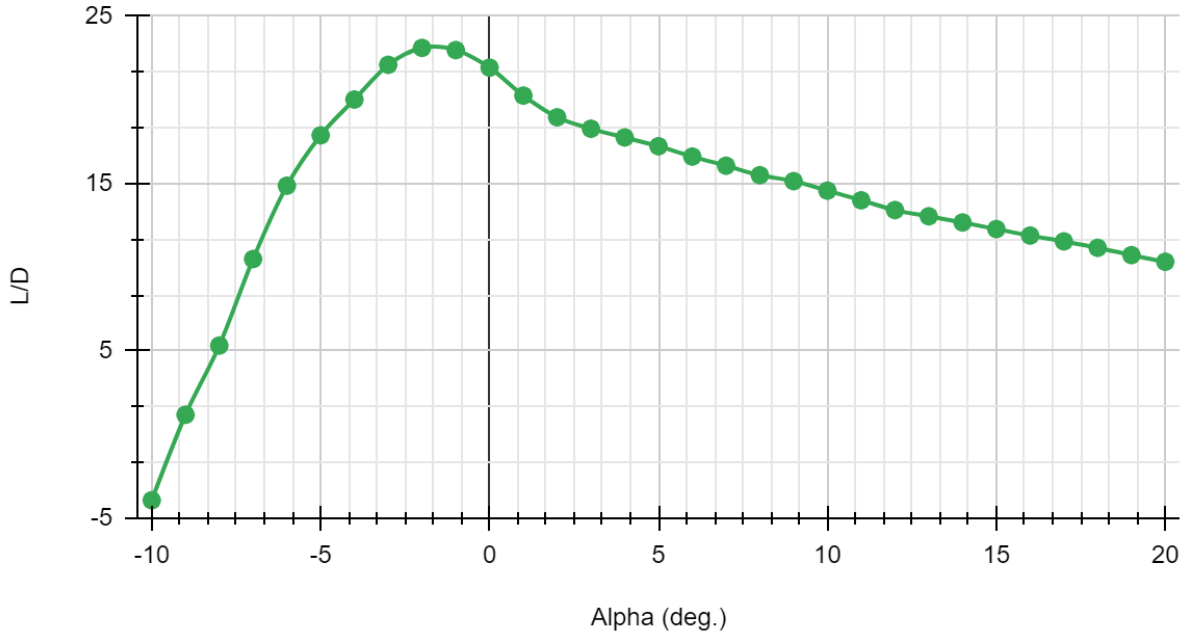


Figure 5.4: Lift over Drag vs Angle of Attack at Takeoff

Takeoff Drag Polar (M=0.17, Sea Level)

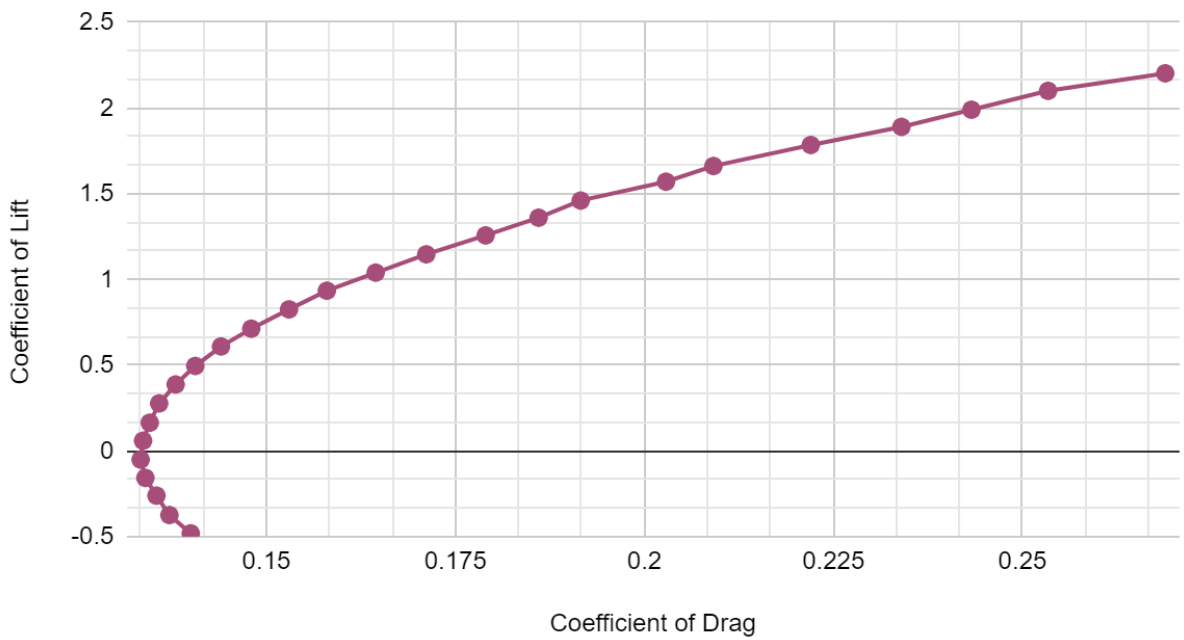


Figure 5.5: Lift vs Drag at an Angle of Attack Ranging from -10° to 15°

Cruise Drag Polar ($M=0.4$, Alt.=30000 ft)

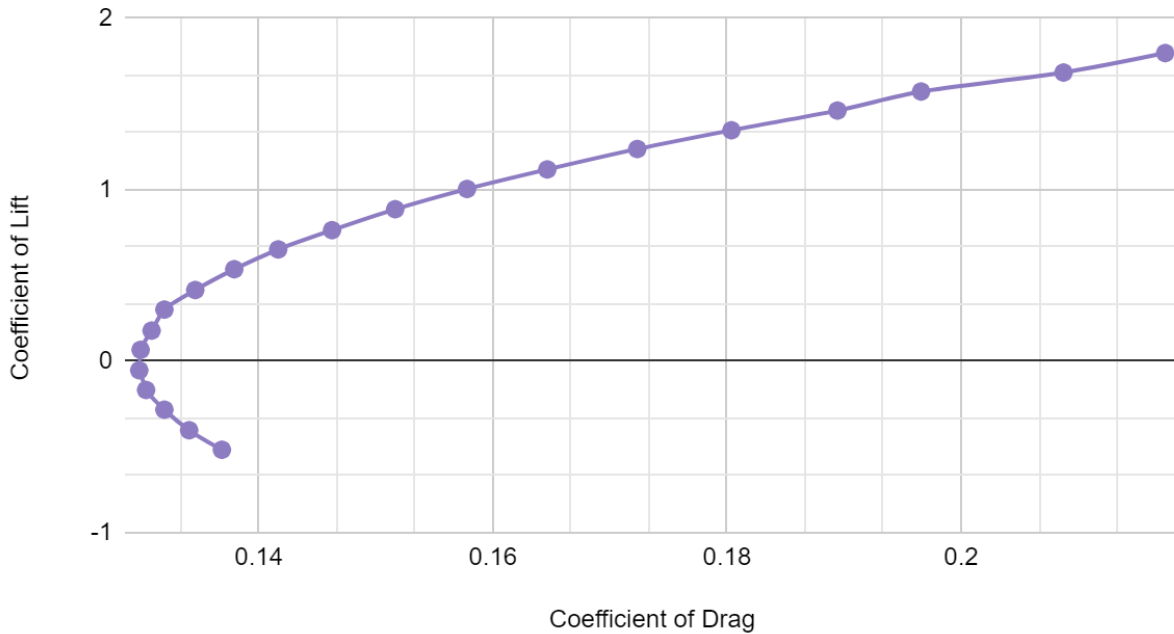


Figure 5.6: Lift vs Drag during Cruise

These studies helped inform the aerodynamic characteristics of our aircraft during takeoff for optimal performance. Studies such as this were conducted across wingspans ranging from 72 ft to 118 ft with varying chords and roots. Eventually, the studies seen above provided the best results clarifying the wing sizing.

Parasitic drag values were calculated using VSPAero and the values are shown in Table 5.2. The highest contributor to parasitic drag is the vertical tail, followed by the wings, fuselage, and propellers. The horizontal tail and electric motors do not contribute significant amounts to the total parasitic drag.

Table 5.2: Parasitic Drag

Component	S_{wet} (ft ²)	C_D	% Total
Fuselage	157.82	0.00666	13.00
Wings	123.75	0.00890	17.37
Vertical Tail	54.82	0.02525	49.29

Horizontal Tail	33.36	0.00234	4.57
Electric Motors	24.33	0.00170	3.31
Propellers	13.87	0.00639	12.47
Total	407.95	0.05124	100

5.4 Empennage Sizing

Table 5.3: Empennage Sizing

VT VSP Geometry Area (ft ²)	C_{mx}	Static Margin (w/ calc. CG)	X_{np} (ft)	Static Margin (CG @ c/4)
398.3	0.0060	-0.0596	114.5	0.3167
387.5	-0.0279	-0.0053	118.1	0.3725
382.1	-0.0089	-0.0191	117.0	0.4101
376.7	-0.0060	-0.1073	110.8	0.2808
375.6	-0.0011	-0.0920	111.7	0.2874
322.9	-0.0014	-0.0982	110.5	0.2913
269.1	0.0005	-0.1252	108.0	0.2774

5.5 High-Lift Devices

The aircraft is equipped with flaps, ailerons, elevators, and a rudder. The trailing edge flaps are single slotted and sized to decrease both the takeoff and landing distance. The single slotted flaps were chosen to reduce boundary layer separation and keep the flow over the top of the wing laminar. Additionally, the single slotted design is easy to build and allows for more accurate and precise analysis.

Flap Sizing

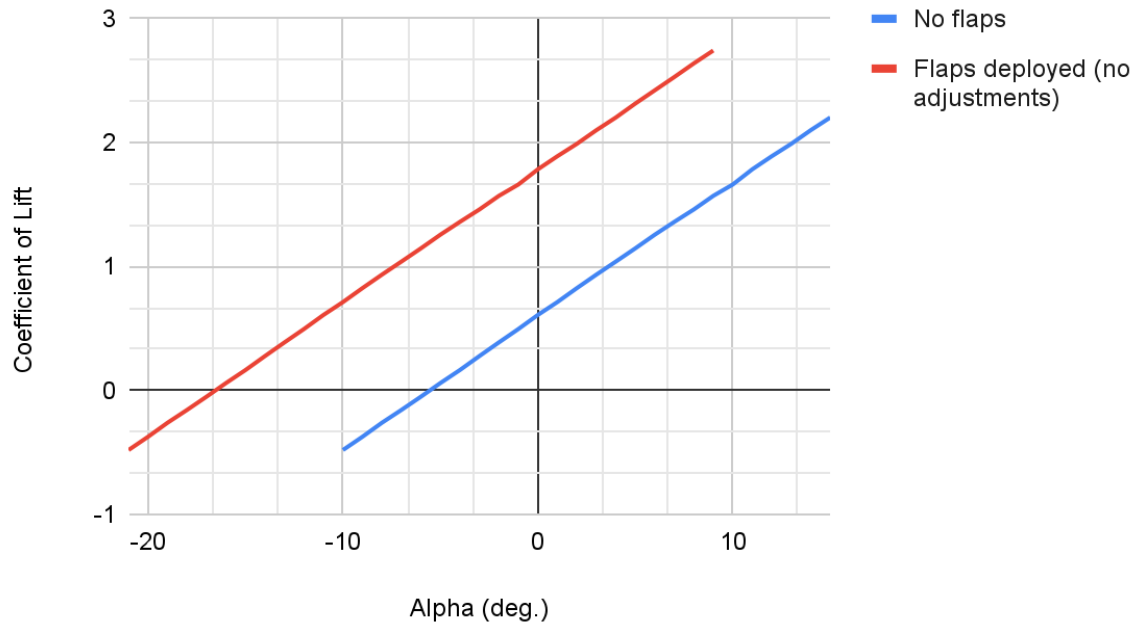


Figure 5.7: Graph for Obtaining Preliminary Values for Flap Sizing

Figure 5.7 shows $\Delta\alpha_{0L}$ is equal to 10.4° and $\Delta C_{l,max}$ equal to 1.28. Using these values and equations from Carichner & Nicolai, a final value for increase in lift due to flaps could be obtained. The value for $\Delta\alpha_{0L}$ was chosen using equation 5.1. $\frac{-d\alpha}{d\delta_F}$ was obtained from Figure 9.11 in Carichner & Nicolai using a flap deflection (δ_F) of 20° and a c_f/c of 0.3.

$$\Delta\alpha_{0L} = \frac{-d\alpha}{d\delta_F} \cdot \delta_F \quad (5.1)$$

After obtaining $\Delta C_{l,max}$ from Figure 5.7 that value could be inserted into Equation 5.2 to adjust for sizing and aerodynamics to determine the increase in lift due to flaps at a 9° angle of attack for takeoff.

$$\Delta C_{L,max} = \Delta C_{l,max} \cdot \frac{S_{WF}}{S_w} \quad (5.2)$$

This yielded a final increase in coefficient of lift at a takeoff angle of 9° from 1.57 to 1.95, a 26.3% increase. The target was a 25% increase to raise our factor of safety at takeoff to 1.25 as well as the previously mentioned decrease in takeoff and landing distances. The final trailing edge flaps are deflected 20° at takeoff and have a chord that is 30% of the wing chord and are located from 10% to 40% of the wing span on each side. Table

5.4 shows the increase in maximum coefficient of lift due to different flap deflections at takeoff conditions as well as the increase in drag for each configuration. The change in drag was calculated using Equation 5.3 where k_1 and k_2 are correction factors based on c_f/c and deflection, respectively.

$$\Delta C_{D,flap} = k_1 k_2 \frac{S_{WF}}{S_w} \quad (5.3)$$

The rudder was sized to produce enough lift to counter OEI conditions when deflected 25° . It is located from 40% to 70% span with a chord ratio of 0.25. The ailerons have the same chord ratio as the flaps and are located from 50% to 80% of the wing span on each side to assist with longitudinal stability and control.

Table 5.4: Changes in $C_{L,max}$ due to Flap Deflection

Flap Deflection (degrees)	New $C_{L,max}$	% Increase	$\Delta C_{D,flap}$
10	1.76	12.0	0.002625
20	1.95	26.3	0.006563
30	2.05	30.8	0.01313

r5.6 Wingtip Propulsor Benefit

By reducing the aerodynamic losses associated with wingtip vortices and downwash, counter-rotating propellers mounted at the wingtip are estimated to reduce the induced drag of the wing by approximately 10% [24]. Additional benefits of wingtip propulsors include reduced cabin noise levels [25] and inertial relief on the wing structure during maneuvering. Although there is significant yawing moment associated with wingtip-mounted propulsors, calculations show that these are easily overcome.

6. Propulsion

6.1 Hybrid-Electric Architecture Comparison

Hybrid-electric technologies are ways of implementing additional electric systems into aircraft that augment efficiency of the system. In a hybrid-electric architecture, this will refer to the system that converts the stored energy of the battery and fuel into propulsive power.

For hybrid-electric aircraft, the main methods of hybridization are turboelectric, parallel hybrid, and series hybrid. Turboelectric aircraft use a gas turbine to run a generator to produce electricity, which then sends the power to electric motors that provide thrust. In a parallel hybrid propulsion system, electric motors supplement the turbines on the aircraft. Series hybrid-electric propulsion systems combine a turboelectric setup with a battery to provide energy for the propulsion system. In these architectures, a variety of electrical components could be needed, such as motors, wiring, AC/DC converters, circuit breakers, and possibly a battery.

In addition to the general types of architectures, there are levels of hybridization that vary from very mild to fully electric concepts, depending on how much energy is sourced from electricity or a battery instead of traditional jet fuel. In mild hybridization concepts, electricity is used to run more of the systems in an aircraft or help supplement the combustion engine, but not replace a large portion of thrust. Conversely, in higher hybridization levels such as a fully electric aircraft, none of the power is supplied by a gas turbine engine and instead, batteries and electric motors provide 100% of the thrust.

One major consideration when designing and selecting a hybrid-electric architecture was the limitation of the fuel sources. Classically, most aircraft in service have used jet fuel with an energy density of approximately 12,000 Wh/kg. Jet fuel has a high specific potential energy, and even if a significant portion of the energy might end up lost as waste heat through inefficiencies in combustion and thermodynamics, the high density of jet fuel compensates for this. Contrasted to other technologies, lithium-ion battery technology will only have an energy density of 500 Wh/kg even by the most optimistic projections for 2034 [27]. As a result, even if the electrical energy that is stored in a battery can be recovered with high efficiency, the low energy density of lithium-ion batteries becomes prohibitive for large batteries due to their heavy weight in an aircraft concept. Other battery technologies such as metal-air batteries and alternative battery chemical formulations were considered due to their higher energy

density values, but many of these technologies do not have the technology readiness levels that were considered viable for an engine system for entry into service by 2034. In addition, fuel cells such as hydrogen-based technologies were considered, but the practicality concerns made them unfeasible [26]. Due to the extensive lack of infrastructure currently at airports to support such technology, it would be extremely cost prohibitive for the airport and commercial airline industry. In addition, such facilities and technology would be prohibitive for some locations such as small islands, due to the lack of infrastructure or resources to build a highly specialized production facility just to service the aircraft. One of the primary design goals was to be able to make the concept marketable and cost effective over a wide range of customers and locations, and this was taken into consideration for our design.

6.2 Propulsion Architecture Comparison

There are two main propulsion configurations: conventional and distributed electric propulsion (DEP). DEP works well with turboelectric systems, as electric motors are lightweight and small; so if power is provided by a central turbine, electric motors can be easily placed all along the fuselage or wing. This can result in benefits such as increasing the airflow passing over the wings due to the distributed propulsors along the wing. As a result, DEP has several advantages such as increased fuel efficiency, better aerodynamic performance when in use, shorter takeoff, and less need to control surfaces as thrust modulation can provide the same effect. It also has several disadvantages such as increased complexity, increased weight, and decreased mechanical efficiency as power is lost when mechanical power is turned to electrical in the generator. In a conventional configuration the turbines provide power with potential for additional power coming from electric motors connected to the turbine. This configuration works well with a parallel hybridization system. Its advantages stem from the relative simplicity of the design as well as the ability to easily implement varying degrees of hybridization. A series parallel system with a more traditional wingtip mounted configuration was selected instead of a DEP configuration. This propulsion architecture led to the greatest impact on fuel burn after analyzing our early conceptual designs.

6.3 Methodology, Calibration, and Reference Propulsion System

As Low Rider's performance baseline is the ATR 42-600, its propulsion system served as baseline for the propulsion system model. The GasTurb software package serves as a quick and effective way to rapidly model gas turbine engines which can be used to calculate several parameters critical to design. Engine thrust is calculated at specified create an engine deck, which can be read by FLOPS and used to calculate aircraft performance. The deck captures a variety of data points that FLOPS can then use to analyze the mission, such as mach number, altitude, total thrust, fuel flow, and NO_x emissions. In addition, GasTurb is able to create a variety of plots to rapidly perform small trade studies using up to three different engine parameters so see how various factors are related.

For the development of our reference gas turboprop engine deck, a baseline PW127 engine used on the ATR42 was used as a reference in order to scale our projections for a next generation turboprop engine that would be ready for service and certified by 2034. To evaluate engine performance, a software package called GasTurb was used and calibrated with the reference engine in order to reasonably match engine performance with reported values by ATR and Pratt and Whitney. While some parameters are not reported by Pratt and Whitney on various specifics of the engine, a NASA study used a similar software package called NPSS in a similar vein of analysis to model and predict the performance of the PW127 engine. These specifications used to model the reference engine are the next section with Table 6.1.

6.4: Gas Turboprop Engine

For our design, a large portion of the power used to provide the thrust of the aircraft comes from our gas turboprop engine, which is based on projections for technology advancements for an engine entry into service by 2034. For our next generation engine, the aforementioned paper on the PW127 and future technology projections was used to estimate the effects of these improvements that were incorporated into our future next generation engine model [27]. In addition to these improvements, some papers suggest a significant improvement in combustion chamber temperature capabilities, as high as 1800 Kelvin, which was the driving force behind our decision to use 3240 Rankine [28]. One issue of going higher than 1800 Kelvin is the risk of generating significantly more NO_x and

emissions above 1800 Kelvin for the designed combustion chamber temperature. In addition, in an interview with Rolls Royce propulsion engineer and Rolls Royce Chief of Preliminary Design David Eames, it was suggested that the 2034 projected pressure ratio used in our model could be significantly increased which would result in significant fuel burn savings. This trend of higher OPR can already be seen in some of the larger turboprop engines currently in service today mainly in the military. However, this came at the detriment of significantly more NO_x emissions. The comparisons in SFC between our current generation engine model and the next generation model are shown below in Figure 6.1 and the contrast in NO_x emissions in Figure 6.2. Note the benefit in SFC correlating to a noticeable increase in NO_x emissions. This increased NO_x generation is influenced significantly by the pressure ratios, although T4 burner temperature does have a smaller effect up until 1800 Kelvin.

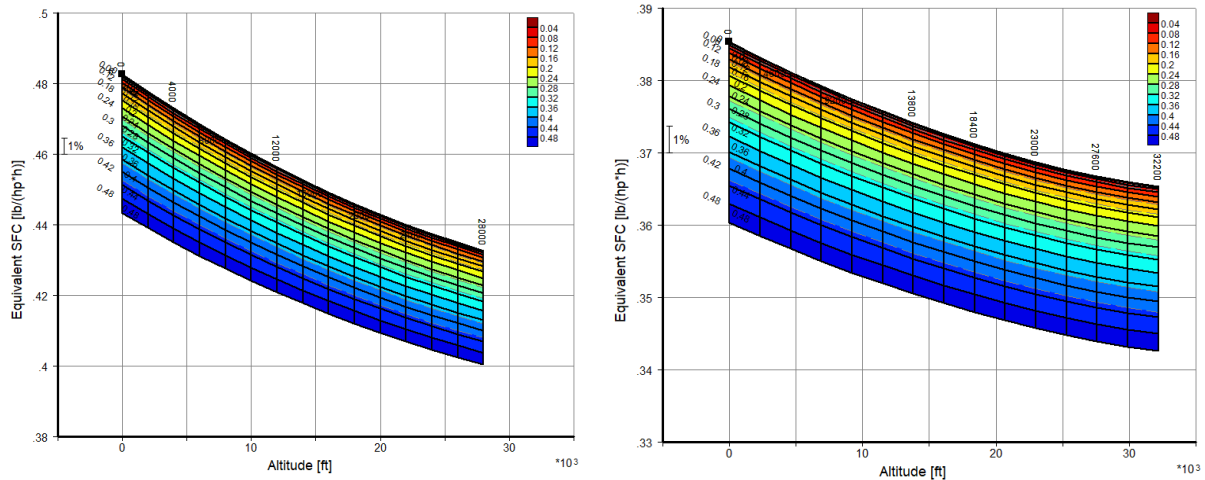


Figure 6.1: SFC Comparison between the Current Generation (left) and Next Generation Engines (right)

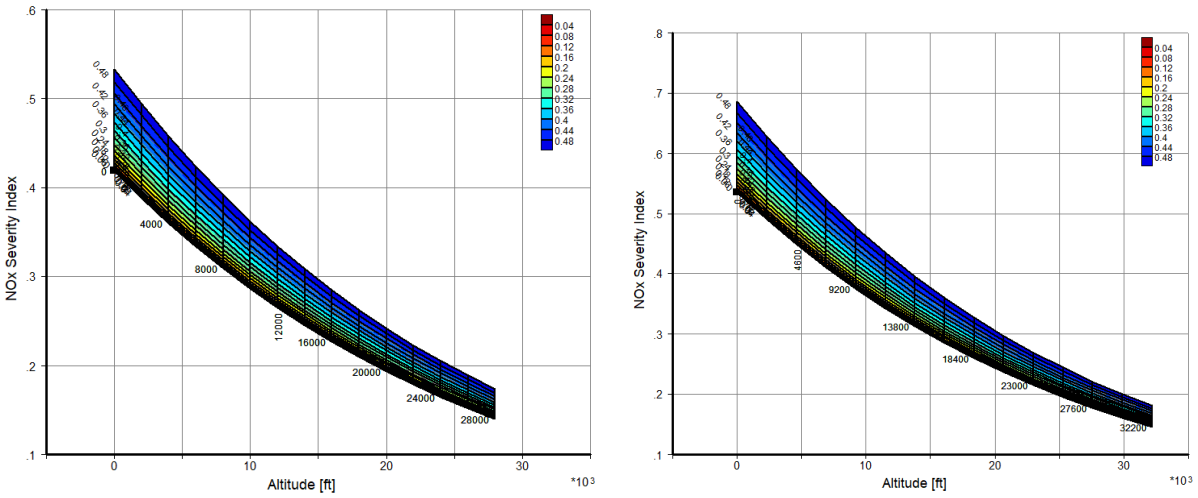


Figure 6.2: NO_x comparison between the Current Generation (left) and the Next Generation (right). NO_x Severity Index depicted here Represents 32g of NO_x Emitted per Kilogram of Fuel Burned.

After performing trade studies involving altitude, NO_x emissions, and fuel burn, it was discovered that flight at 30,000 ft could be beneficial for NO_x emissions while retaining most of the fuel burn benefit as shown in Figure 6.2 previously. In order to achieve a cruise altitude of 30,000 ft, it was discovered that 2,750 SHP was not enough. As a result, the baseline engine was scaled to provide 3,000 SHP which also provides better takeoff performance with more power. While there is an increased weight and SFC associated with this larger engine, the ATR 42-600 was designed to fly almost 10,000 ft lower, and must be run at nearly 90% throttle to maintain even FL280. By running a larger engine at a lower throttle setting at a higher altitude, a reduction in total fuel consumption and NO_x can be achieved.

While there were some technologies that have been suggested such as water injection and other NO_x reducing engine modifications that might significantly reduce the NO_x output of the engine, the decision was ultimately made not to model such systems into the engine design as a limitation of our model analysis. That being said, Sustainable Aviation Fuels (SAF's) were considered for future use, as they have the potential to reduce overall total climate emissions and improvements and proliferation of SAF advancements would be a part of this concept's operation in 2035 [26]. Because of the significant gains in engine efficiency for an increased OPR, it was decided to select an OPR that produces slightly less NO_x than the PW127 in order to reduce total engine emissions and fuel

burn. NO_x emission calculations were performed by FLOPS using engine data, and OPR's from 15.8 to 20.5 were considered on the 500 nm economic mission. Figure 6.3 shows the results of this study.

The ATR 42-600 was projected to produce 22.7 lbs of NO_x on the economic mission. Using these results, an OPR of 19.7 was selected. Though this generates only a small reduction in NO_x emissions of 0.2 lbs, the next-gen engine is now capable of reducing block fuel burn by an additional 5% from the baseline.

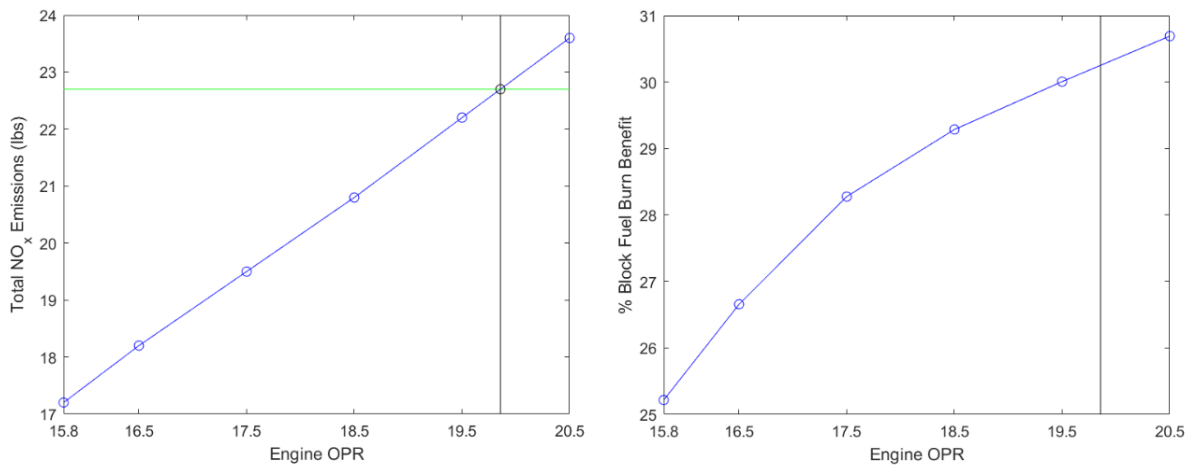


Figure 6.3: Impact of Engine OPR on Total NO_x Emissions and Block Fuel Burn

Below is Table 6.1 showing key characteristics of our modeled engines: the current generation PW127, a next generation PW127 with projected future engine parameters, and a resized version of the next generation engine that has been interpolated linearly to have a reduced weight and appropriate power. In our calculations, it was difficult to accurately predict the weight of our future generation engine, so an additional approximate 10% margin of error was added to the engine weight to account for the interpolation error. This arrives at the approximate 750 lbs used for each gas turbine engine weight. The power to weight ratio of the next generation engine is at around 4.04 hp/lb compared to the current generation 2.62 hp/lb, which is a significant benefit for weight on the wing.

Table 6.1: Engine Characteristics Modeling Results

Inputs:			
	Current Gen	Next Gen	Next Gen (Resized)
Intake Air Flow [lb/s]	18.7	18.7	11.9
Overall Pressure Ratio	15.77	19.7	19.7
Burner Temperature, T4 [R]	2680	3240	3240
Burner Efficiency	0.95	0.98	0.98
Compressor Efficiency	0.85	0.88	0.88
High Pressure Turbine Efficiency	0.85	0.88	0.88
Power Turbine Efficiency	0.85	0.88	0.88
Bleed Air Percentage	~2.5%	~2.5%	~2.5%
Results:			
Mechanical Shaft Horsepower [hp]	2776	4782	3029
Engine Weight [lb]	1060	1060	750
SFC lb/(hp*hr)	0.487	0.383	0.385

6.5 Electric Motor

For our aircraft, the NASA HEMM was selected for our electric motor, which stands for the High-Efficiency Megawatt Motor. While the motor is designed to be readily available by 2035 for the megawatt range of power, our team scaled down the size of the motor using the power to weight ratios in a study done using the HEMM motors in the STARC-ABL concept aircraft from NASA [29]. The end horsepower requirement was selected to be 100 hp, which is roughly 3.3% of our gas turboprop power output. This motor was chosen for its high efficiencies, but also the capability for the unit to be used as both a motor or a generator based on the need.

This dual functionality is essential as our concept aircraft takes advantage of motor's excellent performance during climb for electric climb assist, uses the regenerative braking to recapture energy during throttle back or expend that energy during throttle forward during the cruise part of the segment using an engine control system called TEEM, and utilize more regenerative braking during descent to partially recharge the internal battery. These three methods of energy utilization are discussed in the next section, where an overview of how the propulsion systems play a part in the electrification of the design.

6.6 Propeller Analysis

For propeller analysis, a software package called XRotor was used to model the effectiveness of a propeller system. While there were not a lot of resources available concerning the geometric details of the Hamilton 568F propeller used on the ATR 42/72 family of aircraft to make a baseline comparison, XRotor’s design feature was able to generate propeller geometry based on several inputs. The results of the propeller analysis are shown below in Figure 6.4 which also shows the efficiency of the propeller. The geometry is shown in Figure 6.5.

no. blades :	6	radius(m) :	2.0000	adv. ratio:	0.56102
thrust(N) :	0.134E+05	power(W) :	0.205E+07	torque(N-m) :	0.163E+05
Efficiency :	0.9205	speed(m/s) :	141.000	rpm :	1200.000
Eff induced:	0.9413	Eff ideal :	0.9791	Area(m ²) :	11.78097

Figure 6.4: XRotor Geometry Design Results

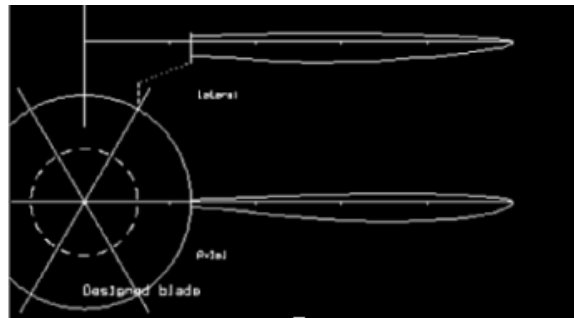


Figure 6.5: Generated Geometry Profiles

While the ATR 42 does include a variable pitch propeller to help with maintaining a more optimal propeller efficiency throughout the different stages of the mission, a more conservative estimate of 90% propeller efficiency was used in the creation of our engine performance deck. This propeller and its efficiency was then used in the GasTurb propeller module to calculate thrust at various mach numbers and altitudes.

6.7 Energy Storage Selection

Several options were considered for electrical energy storage. Although hydrogen fuel cells have a high energy density, their low power density makes them unsuitable for providing sufficient power in short bursts, as required by Low Rider's concept of operations. Additionally, hydrogen has a low volumetric energy density and must be kept at a very low temperature in order to be stored safely. The cost of space and energy required are too great for an aircraft of Low Rider's class to realize the full benefits in addition to practicality concerns [30]. Another storage method considered were the usage of capacitors and related projected technologies. However, those technologies are unproven for use in vehicles and would require too much space in addition to their low energy density to be practical on an aircraft as small as Low Rider and were decided to be unfeasible for appropriate entry into service as an energy storage system by 2035. Despite their shortcomings, Li-ion batteries are the only electrical energy storage system with a proven track record in vehicle application that can provide the power required and have the highest likelihood for entry into service by 2035.

6.8 Battery Sizing Methodology

The primary drawbacks of Li-ion batteries are their weight and limited lifetime. As the energy density decreases, the number of charge/discharge cycles it can withstand increases. In order to maximize battery lifetime, it will be limited to discharging only 80% of its total capacity per cycle [27]. It was decided to size the battery for an expected lifespan of approximately five years. This equates to about 8000 charge/discharge cycles, assuming four flights per day, where each flight is one full charge/discharge cycle. In order to account for capacity degradation over this lifespan, the battery must be oversized by a factor inversely proportional to the lost capacity [27][60].

The battery was sized using a mission energy approach. The fuel required for takeoff and climb was converted into total energy flowing into the engine, and then a percentage of this energy flow corresponding to the propulsion architecture's level of hybridization was used to determine the battery size. The battery was then oversized in order to account for the depth-of-discharge limit and degradation over 5 years. In order to size the battery, FLOPS was used to determine takeoff and climb fuel, which was then input into Equation 6.1 to calculate the required battery size. This was then iterated upon until the segment fuel burns converged.

$$w_{battery} = w_{fuel} \cdot h \cdot \frac{\eta_{thermal}}{\eta_{electric}} \cdot \frac{\rho_{E,fuel}}{\rho_{E,battery}} \cdot \frac{1}{f_{dod}} \cdot \frac{1}{f_{deg}} \quad (6.1)$$

In order to minimize battery weight and maximize fuel burn benefit, the batteries were sized for takeoff and climb on the economic mission. This ensures they will provide enough power for shorter missions. Although the batteries will provide insufficient power to climb to altitude for missions greater than 500 nm, these missions are expected to be the exception rather than the rule for Low Rider, and thus not worth the additional weight required.

In order to determine the battery energy density that would minimize its weight, a study was conducted that estimated battery weight as a function of hybridization and energy density, where energy density was assumed to be linear with battery density. Using the methodology described above and accounting for lost capacity over five years, a battery energy density of 370 wh/kg was determined to minimize the battery weight for any given hybridization level which can be seen in Figure 6.6.

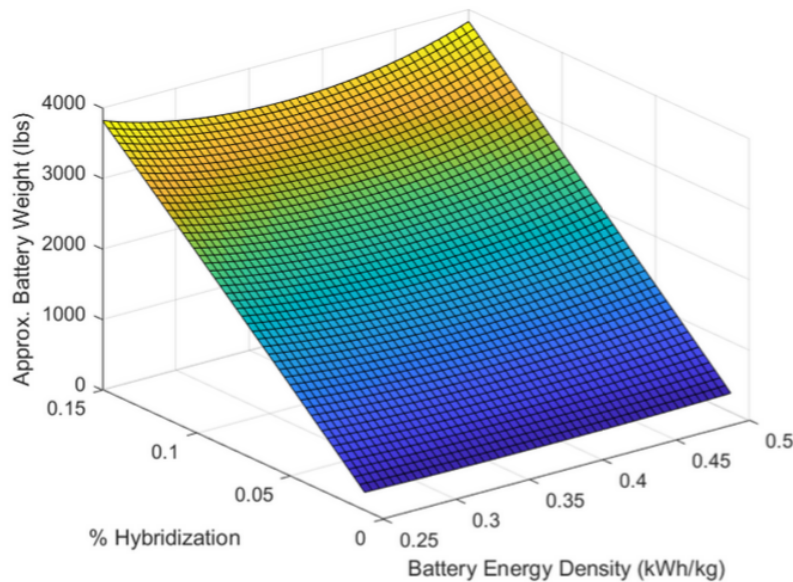


Figure 6.6: Impact of Battery Power Density and Hybridization Level on Battery Weight for Sufficient Battery Storage after Five Years

6.9 Hybridization Trade Study

With the battery energy density selected, a trade study was conducted to determine the optimal level of hybridization. Several FLOPS models were developed for aircraft with hybridization ranging from 0 to 10 percent. The batteries were then sized for the economic mission, and the fuel savings relative to an equivalent aircraft with 0% hybridization were calculated, plotted manually, and analyzed. Figure 6.7 shows that a hybridization of 1% during takeoff and climb resulted in the greatest amount of fuel savings, at 0.5% relative to the non-hybridized case. While the benefit is small, it does justify that the architecture will bring additional fuel burn reductions despite the increase in added weight to the aircraft.

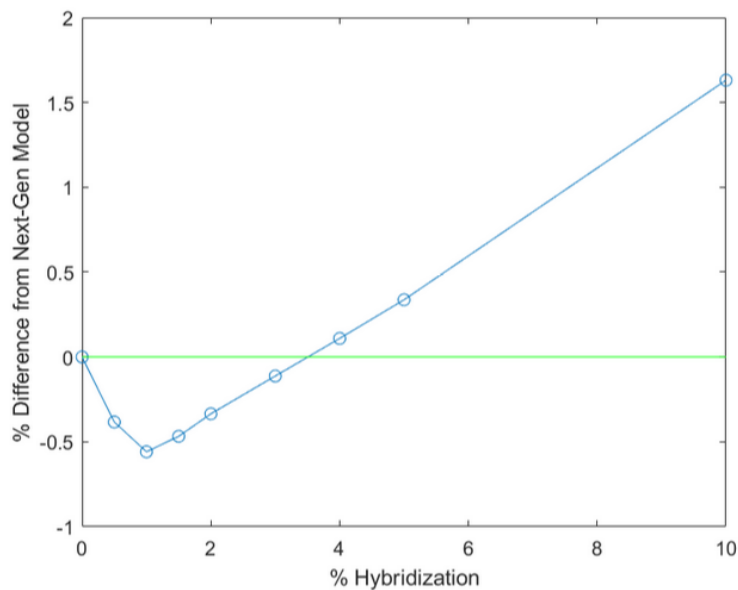


Figure 6.7: Fuel Burn Change Relative to the Next Generation Model at Different Levels of Hybridization

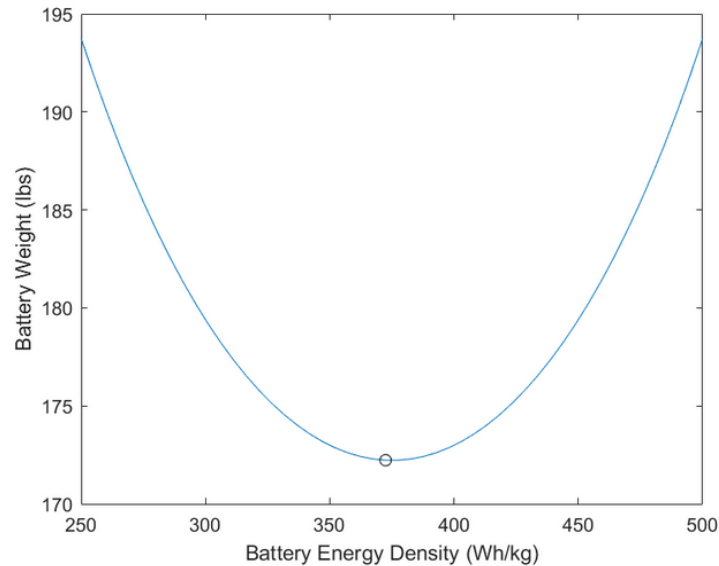


Figure 6.8: Energy Density at 1% Hybridization Effect on Battery Weight

Figure 6.8 above shows a slice of Figure 6.7 at $h=0.01$. For 1% hybridization, the difference in weight between a 250 Wh/kg and 500 Wh/kg battery was estimated to be approximately 20 lbs. In order to determine the sensitivity of performance to the battery energy density assumptions made, FLOPS models using the minimum and maximum battery weights were analyzed. It was found that there was less than a 1 lb difference in block fuel burn between these two cases, which is an order of magnitude lower than the projected benefit of 1% hybridization. The battery weight for Low Rider was thus determined to be 175lb as seen in Figure 6.8. It is important to note that this battery is sized and meant mainly for propulsion only. The electricity for the electronics, lights, and computers are powered using a separate regular sized battery. The size of the electronics specific battery is accounted for and sized separately using FLOPS.

6.10 Electrical System

The electric system to support the propulsion architecture consists of five main components: the propulsion battery, a DC circuit breaker, a DC-AC converter, two AC circuit breakers, and the two HEMM motors on the wingtips. The electric motors and AC circuit breakers will be mounted on the wing, with the electric motors on either wingtip and the AC circuit breakers close to the root of the wing. The AC-DC converter will be positioned on

the inside of the fuselage in between the wings. The battery will be mounted near the middle of the wing root along the centerline of the fuselage. The DC circuit breaker will be positioned between the AC-DC converter and the battery. All of these components will need to be accessed via maintenance panels likely on the underside of the aircraft. In addition, according to a NASA paper on battery sizing considerations for an aircraft, the additional structural weight is extremely small compared to the additional weight due to the scaling of the energy storage system. Since the propulsion battery is relatively light at only 175 lbs, it was determined that at most only a few extra pounds of structural weight would need to be dedicated to housing the battery in the aircraft [27]. The sizing of the other electrical systems is based upon a study that electrifies the STARC-ABL aircraft with improved systems [29]. This can be seen below in Table 6.2 as well as the electrical architecture propulsive efficiency. Both the gas turboprop engine and electrical architecture interface with the propeller discussed in section 6.6 to determine each respective total propulsive efficiency.

Table 6.2: Electrical Component Sizing Specifications

Component	Number	Weight (lb)	Waste Heat Generation (hp)	Propulsive Efficiency
Battery	1	175	13.16	0.999
Circuit Breaker	1	0.296	0.317	0.995
DC-AC Converter	1	5.44	0.630	0.98
AC Cable Bundle	1	6.66	0.998	0.984
Circuit Breaker	2	0.144	0.307	0.995
HEMM Motor	2	14.33	3.00	0.985
Total		201.87	18.41	0.939

While the aircraft is descending to land, the electric motors will be used as generators to recharge the battery by siphoning off the excess power. The charging rate will be limited to a rate of 1C to limit the degradation of the battery. This means assuming a descending timespan of approximately 30 minutes, the battery will be approximately half charged upon the time that the aircraft lands. The aircraft will then finish charging the battery at a rate of 1C on the ground resulting in a turnaround time of 30 minutes to charge the remaining capacity of the battery at a power draw rate of around 30 kW. In comparison, the lowest power Tesla Superchargers charge at 100 kW, with some going up at 250 kW [31]. This means that no complex charging infrastructure would need to be

constructed and only minor modifications would suffice, and it is expected that electrical infrastructure will continue to progress with current trends for renewable electricity.

6.11 Thermal Management System

The TMS is broken down into two subsystems based on temperature needs. The battery needs to be kept at a cooler temperature of below 35°C to reach optimal battery lifetime, while all other electrical systems need to be kept at at least 54°C. We are basing the sizing of the higher temperature TMS on the STARC-ABL HEATheR sizing [29] and the sizing of the lower temperature TMS system in a study that looked at various types of TMS for a battery powered hybrid-electric aircraft [32].

The low temperature subsystem uses thermoelectric cooling modules to cool and heat the battery. The modules have a relatively low COP of 1.33, but a high efficiency of 1 kg per kW of heat dissipated. They were chosen over other methods of cooling because they will only be needed for a small subset of the flight and only when ambient temperatures are above 25°C, therefore the low efficiency is offset by the light weight of the cooling method. Furthermore, most forms of cooling only provide cooling, while thermoelectric modules can provide both cooling and heating.

The higher temperature subsystem used outer mold line cooling using heat pipes located on the skin of aircraft. It has a ratio of weight to power dissipation of 0.6 kg per kW of heat dissipated, while producing no parasitic drag or power draw. This puts the density below conventional methods using fans and pumps of around 0.29 kg per kW, but these systems use power to operate and induce parasitic drag. A study on the STARC-ABL aircraft found that using outer mold line cooling reduced block fuel burn by 0.8% over conventional methods of thermal management systems. The high temperature subsystem is then used to cool the high temperature output from the low temperature subsystem [29].

The thermal management systems are sized to worst case cooling with ambient temperature of 57°C and a battery discharge of 2C. With these parameters taken into account the battery thermal management systems weigh 9.8 kg with a power draw of 12 kW, while the high temperature subsystem has a total weight of 18.1 lbs. This results in a total TMS weight of 39.7 kg.

The sizing of the battery and level of hybridization gave a battery output of 76.5kW during the 30 minute period of takeoff and climb. Since the motors are upsized by around three times to support TEEM, the total weight of the electrical system comes in at around 202 lb, with a heat dissipation need of 18.8 hp due to inefficiencies throughout the system.

6.12 Final Design Architecture and Claimed Benefits

The three main techniques used in Low Rider's propulsion architecture are electric takeoff and climb boost, TEEM, and regenerative braking.

The first strategy used is electric takeoff and climb boost, where roughly 1% of engine's power is supplied by the electric HEMM motor and an internal battery pack sized to provide just enough energy for the climb segment of our mission. As mentioned previously, the 1% hybridization was chosen due to the fuel benefit found during mission analysis to give the most benefit for our design and level of assumptions made for technology readiness for the components of our design. Some of the major driving design factors behind this 1% hybridization was the effectiveness of our battery, which had considerations with battery life, maximum capacity, discharge depth, and energy density which severely limits the effectiveness of our design.

For our second strategy to further decrease fuel consumption, we are using TEEM engine throttle control, which stands for Turbine Electrified Energy Management. The premise of TEEM is in the utilization of the electric HEMM in order to manage the engine cycling during throttle and throttling of the gas turbine. Since the HEMM motor is significantly more responsive to changes in throttle, the motor would be able to assist the gas turbine so that it could maintain a more constant or optimal operation. This might mean recapturing some of the energy using regenerative braking, or expending that energy in the battery [33]. This is also the reason why the HEMM motor was upsized beyond the 1% hybridization level of 27.5 hp up to 100 hp in order to capture a larger percentage of throttle ranges during cruise. Utilizing TEEM in our design nets an approximate 0.75% benefit in overall TSFC according to a study done on the benefits of utilizing electric motors with conventional engines.

Regenerative braking is the final part of the electrification strategy, as it will be used to capture some of the excess power during descent to recharge some of the battery. The goal of regenerative braking during descent is to

partially reduce the charging time on the ground. This technology is readily used in several applications for trains and cars, and due to the small size of our battery, which is sized for only 1% of the energy needed during climb, that our 100 hp motor would be able to capture a large portion of the energy needed for the next flight. As mentioned previously, we would expect less than an hour for the aircraft turnaround time for the battery to be fully charged.

6.13 Potential Future Technology

In the early stages of our project we looked into using an external battery and motor to propel the aircraft during taxi and takeoff, so the turbine engines could be run at idle. This resulted in a fuel saving of around 2.5% based on FLOPS. For this technology to work the airport would need to have a battery and propulsion system that it would connect to the aircraft before taxing, that would be left on the runway when the aircraft took off. The turbine would be kept off during taxing and kept on idle during takeoff. We decided not to pursue this technology because it required airports to have the specific system needed for our aircraft, greatly limiting where our aircraft could takeoff from. This decision was greatly influenced by our goal to make an aircraft that could fly into the large number of small airports around the world that are under utilized.

Currently car manufacturers are planning to implement solid state batteries in cars by 2030. With this in mind, our group anticipates that such solid state batteries will be available by 2040 in time to replace the aging batteries in our aircraft. These solid state batteries have greater power density and less degradation than conventional lithium ion batteries, meaning that the battery will only need to be replaced once over the lifetime of the aircraft.

7. Structures

7.1 Fuselage Frame

For the fuselage, the Pultruded Rod Stitched Efficient Unitized Structure, or PRSEUS, was selected. PRSEUS is an advanced composite structure developed by the NASA Langley Research Center. PRSEUS was selected due to its combination of light weight and strength. According to FEM analysis, NASA determined that a cylindrical fuselage constructed with PRSEUS would have a weight of 12.76 lbs per square foot of floor area,

compared to 14.73 lbs per square foot of floor area for a conventional aluminum fuselage. This represents a 13% weight reduction for the hybrid-electric turboprop regional concept's fuselage. The thickness was calculated using the maximum allowable hoop stress and axial stress. Because PRSEUS is an anisotropic material, it has significantly different performance depending if it is stressed in the longitudinal or transverse direction. In the longitudinal direction, the ultimate strength of PRSEUS is 105.1 ksi, whereas it is only 46.5 in the transverse direction [34]. Therefore, both the hoop and axial stresses must be considered, because the maximum allowable stress for each will be different. The set of Equations 7.1 was used to calculate the required thickness for each direction. A safety factor of 1.5 was applied. The pressure used was 10.92 psi, which corresponds to a cabin pressurization of 8,000 ft.

$$t_h = \frac{P_i \cdot r}{\sigma_{h,max}} \quad t_a = \frac{P_i \cdot r}{\sigma_{a,max}} \quad (7.1)$$

From these formulas, it was determined that the required thickness for the maximum hoop stress was 0.007 inches, whereas the required thickness for the maximum axial stress was 0.008 inches. Therefore, the required fuselage thickness is 0.008 inches to account for the axial stress of PRSEUS in the transverse direction.

7.2 Wing Box

For the ribs, spars, and stringers of the wing, the material selected was the aluminum 7075-T6 alloy for its low density and high yield strength. For the wing skin, the material selected was carbon-fiber reinforced polymer. Aluminum 7075-T6 was selected because of its high yield strength and strength to weight ratio, allowing it to bear the required loads while being as light as possible. Although composite materials such as carbon-fiber reinforced polymer are more expensive and difficult to manufacture and maintain, it was selected for the wing skin in order to reduce weight, and in turn, block fuel burn. Additionally, airlines have been flying and maintaining aircraft with a significant amount of composite components for many years. Therefore, it was determined that the target market would be familiar with the material by the 2035 entry into service date. Additionally, with this increased knowledge, the price to manufacture and maintain composite material is anticipated to decrease to be more comparable to aluminum by 2035. The material properties of both materials are shown in the table below.

Table 7.1: Aluminum vs Carbon Fiber

Property	Aluminum 7075-T6 [35]	Carbon Fiber Reinforced Polymer [36]
Density (lb/in ³)	0.102	0.051
Yield Strength (psi)	73,000	137,000
Ultimate Strength (psi)	83,000	146,000
Young's Modulus (ksi)	10,400	13,800

A box beam was utilized for the Low Rider's wing structure, consisting of two spar caps along the upper and lower surfaces of the wing and two shear webs on the sides. This design reduces the critical Von Mises stress caused by the spanwise bending of the wing due to the distributed lift force. At this point, the design was iterated upon until a safety factor of 1.5 was achieved throughout the wingbox with minimal weight.

The Low Rider is able to claim a structural benefit from the wingtip propulsor as it provides relief to the wing during high-g maneuvers. As the wing of an aircraft in flight can be modeled as a cantilever beam with a distributed load from the lift force, it experiences a very high internal moment and internal shear near the root. However, the outboard location of the wingtip propulsor significantly reduces the internal moment experienced by the wing. Therefore, the weight of the wing structure can be reduced compared to a structure with a conventional engine placement.

Z stringers were selected for use on this concept. This style was selected due to its optimal combination of low weight, high structural efficiency, and high corrosion inspectability as outlined in Niu [37]. The skin thickness is 0.2 inches, which is comparable to other aircraft in the Low Rider's class.

The Low Rider has 20 ribs which are unevenly spaced as there are three sections of the wing with different sweep and taper characteristics. The spacing in each section increases, with the ribs being spaced 19.8 inches apart in the inboard section (the first 5 ft of the wing from the fuselage), 23.8 inches apart in the middle section (5 ft to 15 ft from the fuselage), and 31.5 inches for the outboard section (15 ft from the fuselage to the wingtip). A comparison with a conventional regular spaced wing with 20 ribs was conducted. It was determined that unevenly spacing the ribs as described significantly decreased the maximum stress experienced by the wing, allowing the spar web thickness to be decreased from 0.59 inches to 0.51 inches, resulting in a 1.5% weight reduction for the structure.

Weight reduction was performed on the wing structure as outlined in Niu [37] in order to reduce weight while maintaining structural integrity. This was accomplished by extruding holes in the ribs in order to reduce weight while maintaining required rigidity. Five holes were placed in the wing, at 8%, 25%, 36%, 47% and 61% chord. The diameter of the holes are 5.9 inches for the first three holes, 4.9 inches for the fourth hole, and 3.9 inches for the fifth. The location and size of each hole was chosen so that neither the rib nor its interaction with the box beam would create a thin region which would compromise the structural integrity of the wing box.

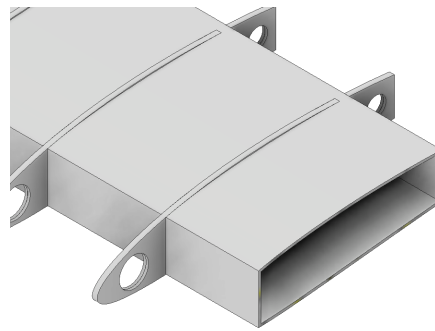


Figure 7.1: Box Beam Cross-Section

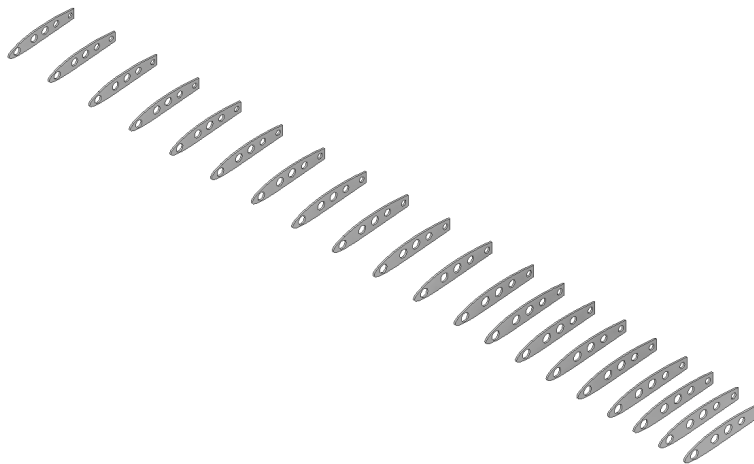


Figure 7.2: Rib Layout of Wing

FEA was performed on the wing to ensure that it would be able to withstand all loads called for in the flight envelope, as well as the weight of the wingtip propulsor. An elliptical lift distribution was used to model lift and an appropriate point load was applied on each rib. A rectangular distribution was used to model the drag, which was resolved to a single point load. A point load applied on the outermost rib was used to model the weight of the propulsor. The critical lift condition used for FEA was determined by multiplying the MTOW by the maximum load factor from the flight envelope. After FEA was performed, it was determined that the maximum stress experienced by the wing at this critical condition was 42 ksi, which satisfies the 1.5 safety factor requirement prescribed by the Part 25 regulations. Additionally, the wing does not displace an inordinate amount, with only 12.4 inches of displacement at the wingtip.

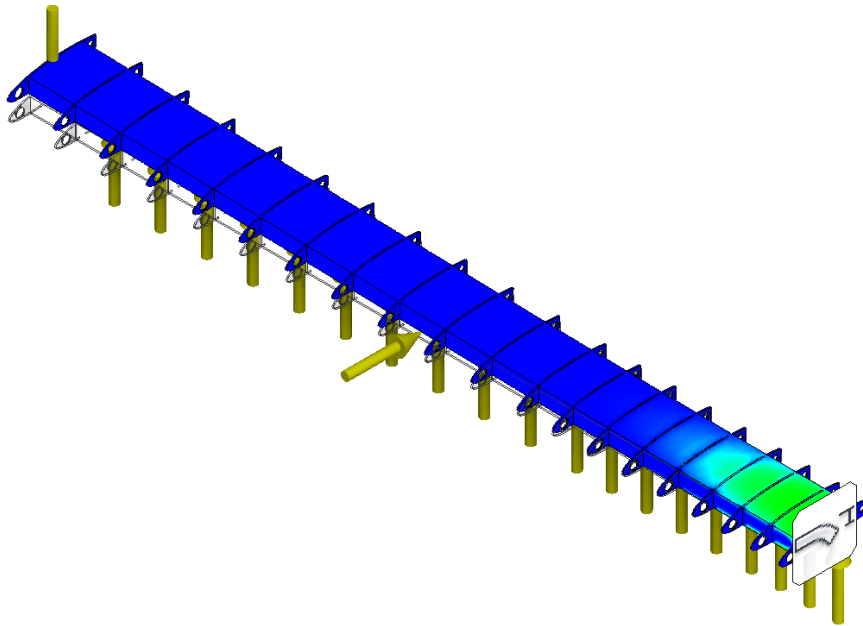


Figure 7.3: FEA of Von Mises Stress

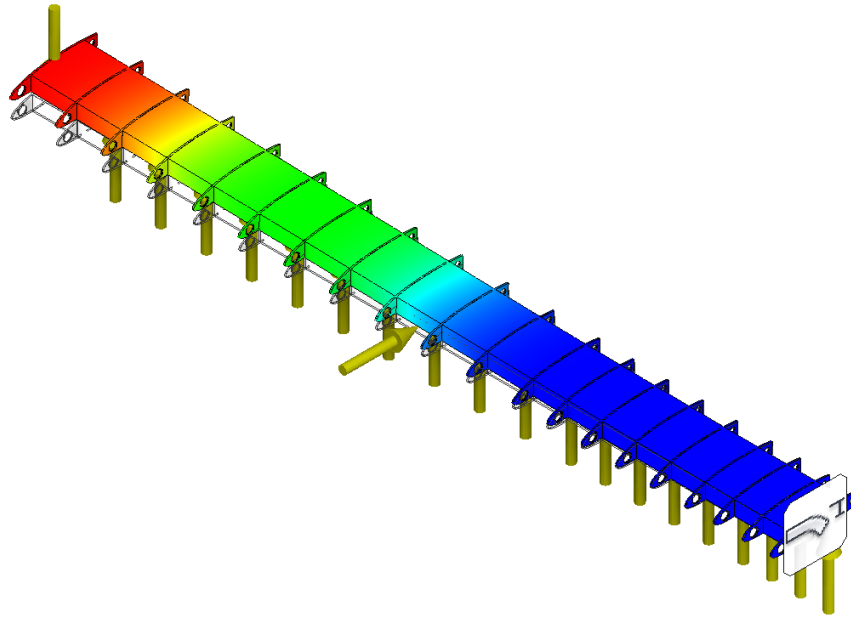


Figure 7.4: FEA of Displacement

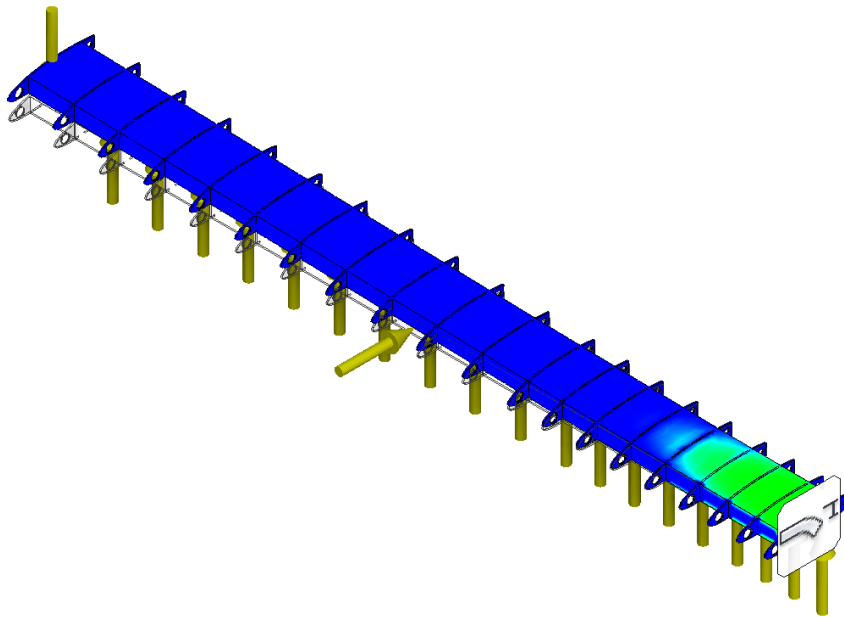


Figure 7.5: FEA of Safety Factor

7.3 Fuel Tanks

The fuel tank is designed to hold 4650 lbs (689 gallons) of fuel, approximately 50 lbs more than required by the design mission. It will be located within the wing, similar to traditional aircraft. The fuel tank is designed to have an inner, outer, and surge tank on each wing. It will also have a central connector to ensure two separate fuel ports are not needed. The left wing will have a pressurized refuel port. Finally, there is no central fuel tank located below the fuselage since the aircraft does not need the extra fuel.

Fuel pumps are often included on aircraft to maintain a continuous supply of fuel at a constant pressure. However on the Low Rider, they are a necessity due to the placement of the engines. Because the Low Rider utilizes wingtip propulsors, and its wings have a positive dihedral angle, gravity feeding of the engines is not possible as the engines sit above the fuel tank. The Low Rider's primary fuel pump is powered by the engines themselves. However, a system of electric boost pumps will supplement the primary pump's function by pumping fuel into the engines for the start, transferring fuel between tanks to maintain balance, and operating during climb and maneuvers in order to maintain constant fuel pressure [38].

Table 7.2: Fuel Tank Parts

Part Number	Part
1	Right Inner Tank
2	Left Inner Tank
3	Right Outer Tank
4	Left Outer Tank
5	Refuel Port
6	Central Connector
7	Surge Tank

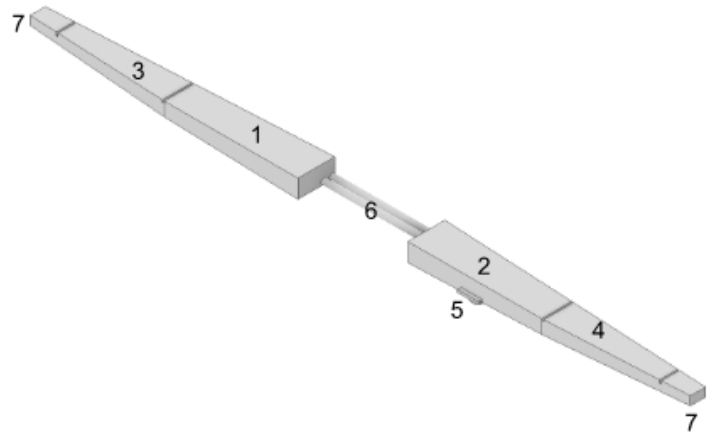


Figure 7.6: Fuel Tank Parts Visual

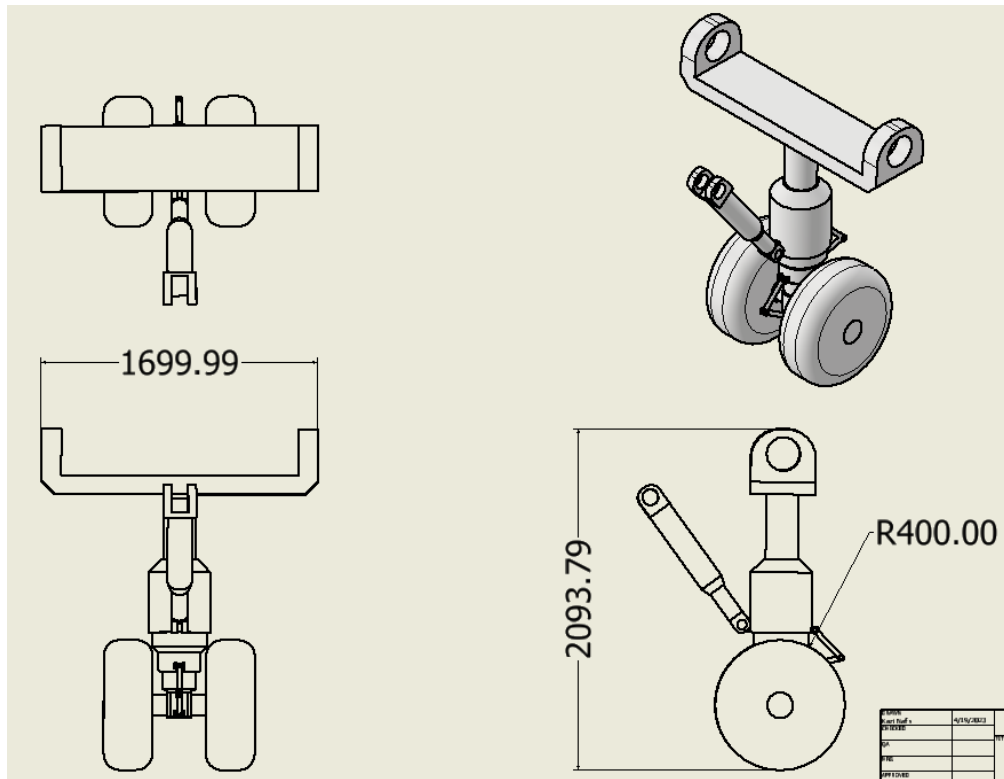
7.4 Landing Gear

7.4.1 Landing Gear Design

The aircraft uses standard hydraulically operated landing gears. There will be two main landing gears and one front landing gear. All landing gears will be equipped with two wheels. The deployment, brakes, and retraction systems will all use hydraulics. The main landing gears will be located on pods under the wings and the front landing gear will be located in the main body. All landing gears will deploy and retract towards the body. The landing gear positioning was influenced by the landing gear position of the SAAB 2000, and placed just behind the aft CG limit. The general design of the landing gear was influenced by the ATR 42-600 and SAAB 2000. The final landing gear design has a maximum height of 2.093m and a maximum width of 1.7m which makes it short enough to fold into pods located on the wing. The front landing gear has the option to include a gravel kit, which will prevent rocks and gravel from hitting the airframe. The main landing gears function structurally similar to the front gear but have larger wheel diameters to assist with spreading the weight during landing and provide sufficient propeller clearance.

Table 7.3: Landing Gear Parts

Landing Gear Parts	
Part Number	Part
1	Wheels
2	Hydraulics
3	Torque Links

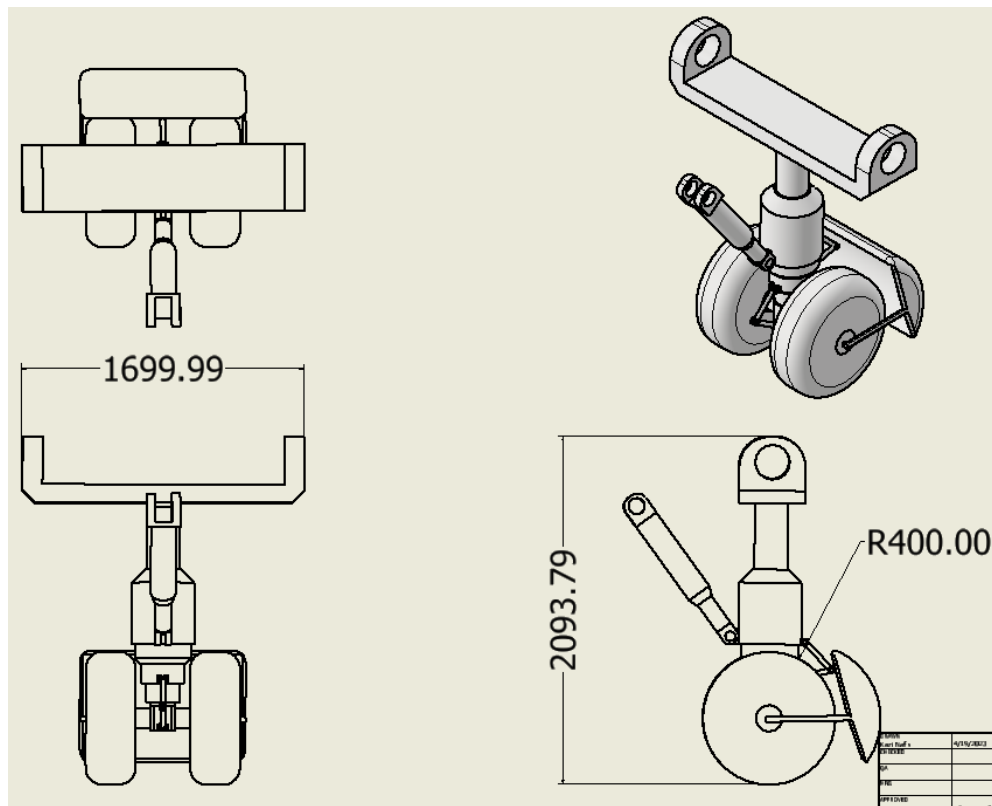


Figures 7.8 and 7.9: Front Landing Gear without Gravel Kit

7.4.2 Gravel Kit

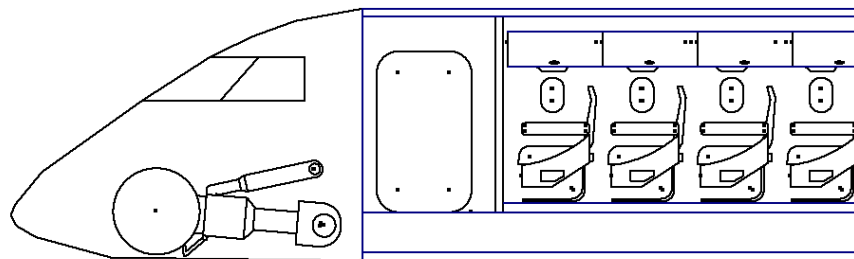
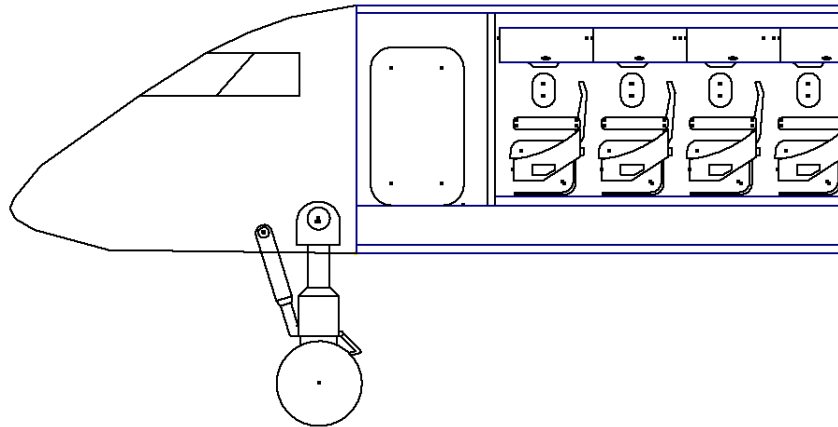
Table 7.4: Landing Gear Parts with Gravel Kit

Front Gear (with Gravel Guard) Parts	
Part Number	Part
1	Wheels
2	Hydraulics
3	Torque Links
4	Gravel Guard



Figures 7.10 and 7.11: Front Landing Gear with Gravel Kit

In remote or underdeveloped regions, access to paved runway surfaces can be limited. To allow for rough-field operations, Low Rider can include an optional “gravel guard” mounted on the front landing gear. This will catch and deflect any debris kicked up from the front wheels, preventing damage to the lower fuselage. The main gear do not require this precaution, as the wings are too short for debris from the wheels to hit them [39].



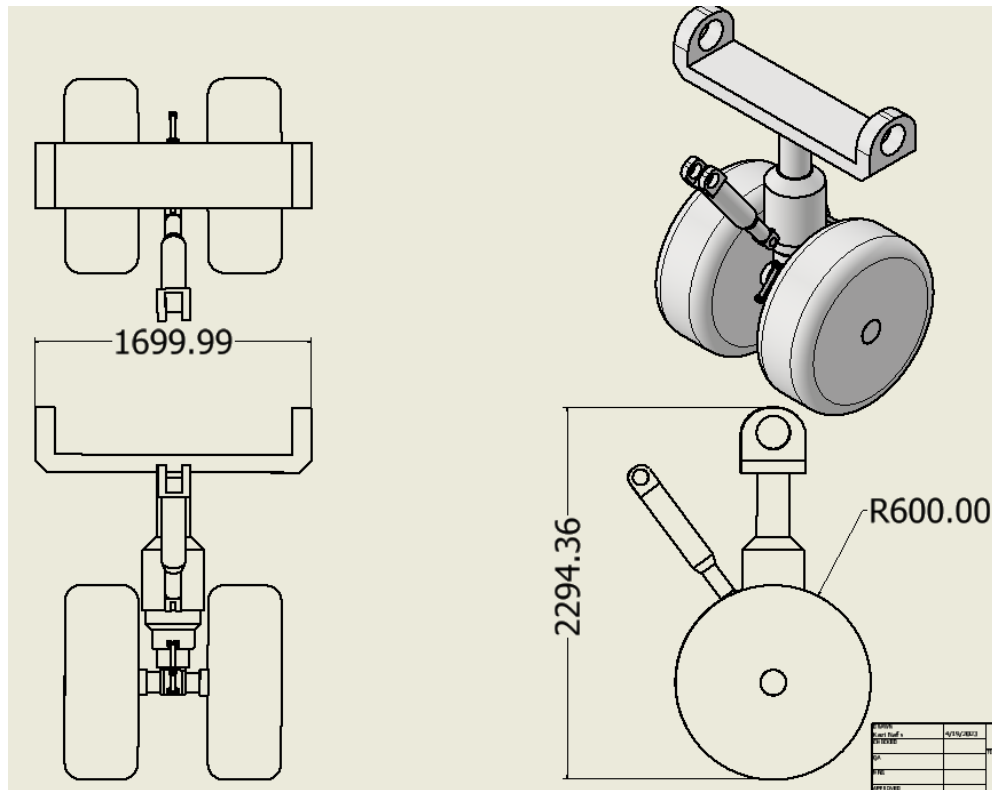
Figures 7.12 and 7.13: Landing Gear Retraction

7.4.3 Main Gear

Table 7.5: Rear Landing Gear Parts

Rear Landing Gear Parts	
1	Wheels
2	Hydraulics
3	Torque Links





Figures 7.14 and 7.15: Rear Landing Gear

8. Weight and Balance

8.1 Final Weight Estimation

The Low Rider FLOPS model was used to estimate the weights of its primary components. Weight reductions were applied to the control system, fuselage structure, and interior plastics and furnishings. These reductions are discussed in greater detail in their respective sections. A 250 lb empty weight margin is included in the weight estimation to account for unpredicted growth in system and structural weights.

Table 8.1: Component Weights and Approximate Locations

Component		Weight (lbs)	% Gross Weight	Distance from Nose (ft)
Structures	Wing	4,187	11.2	28.80
	Horizontal Tail	719	1.9	78.75
	Vertical Tail	403	1.1	74.56
	Fuselage	4,227	11.3	33.79
	Landing Gear Avg	1,262	3.4	23.52
	Nacelles	189	0.5	28.80
	Paint	168	0.5	-
Propulsion	Powerplant + TMS	2,061	5.5	28.80
	Misc Systems	159	0.4	32.72
	Fuel Tanks + Plumbing	143	0.4	32.00
	Battery	175	0.5	28.80
Systems and Equipment	Surface Controls	478	1.3	32.72
	Instruments	134	0.4	6.55
	FBL / PBW	278	0.7	28.80
	Electrical	1,004	2.7	28.80
	Avionics	572	1.5	6.55
	Furnishings + Equipment	2,209	5.9	31.21
	Air Conditioning	323	0.9	30.50
	Anti-Icing	94	0.3	32.72
Operating Weight	Flight Crew + Baggage	660	1.8	8.00
	Unusable Fuel	223	0.6	28.80
	Engine Oil	58	0.2	28.80
	Passenger Service	701	1.9	13.25
	Cargo Containers	525	1.4	33.25
	Empty Weight margin	250	0.7	-
Payload	Passengers	9,600	25.7	32.11
	Passenger Baggage	1,920	5.1	70.00
Mission Fuel		4584	12.3	32.00
Gross Weight		37,306	100	-

8.2 CG Location

Using these weight estimates, the CG limits were then calculated for stability analysis and empennage sizing. The calculated CG envelope can be found in Table 8.2 and Figure 8.1.

Table 8.2: Weight vs CG Location

Loading Condition	CG Location (ft)	Weight (lbs)
Full Payload, Zero Fuel	33.04	32,722
Full Payload, Full Fuel	32.91	37,306
No Payload, Zero Fuel	30.12	21,202
No Payload, Full Fuel	30.45	25,786

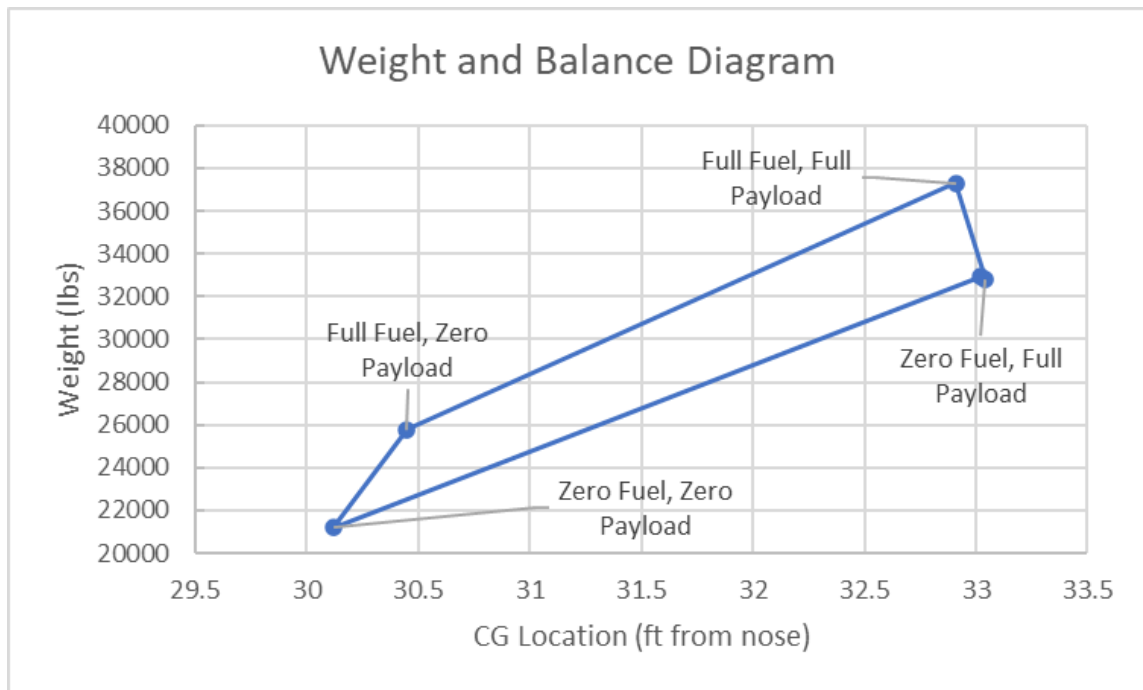


Figure 8.1: Weight and Balance Diagram

9. Stability & Control

9.1 Empennage Design

Empennage sizing was primarily determined by the effect of the vertical tail on the static margin of the aircraft, with a target static margin on the aft CG limit of at least 0.10. The vertical tail was the primary concern for sizing due to it likely having to be a large size to account for the high aspect ratio wings with tip-mounted engines of the aircraft. To determine the most optimal empennage for the aircraft static margin, an iterative process was used where the surface area of the vertical tail was changed by several increments and the static margin calculated for each empennage area using the equations found in Chapter 16 of Raymer. To acquire the neutral point and MAC numeric values required for the static margin calculation, a VSP AERO stability analysis was conducted for each empennage area.

Table 9.1: Vertical Tail Sizing

VT VSP Geometry Area (m ²)	X _{np} (calc)	Static Margin
37	10.4002614	0.121
36	10.6067523	0.154
35.5	11.3783951	0.31
35	10.2968653	0.110

The CG location for the static margin calculation is 32.9 ft from the nose of the aircraft. From this analysis, an empennage with a vertical tail surface area of 35 m² (377 ft²) was found to be optimal.

Once the vertical tail had been sized, the horizontal tail for the empennage was sized based on the horizontal tail size's effect on the coefficient of moment along pitch axis during flight (C_{My}). The goal was to find a horizontal tail size that minimized the moment coefficient. An iterative process similar to that used for sizing the vertical tail was used.

Table 9.2: Horizontal Tail Sizing

Horizontal Tail Area (m ²)	C _{My}

15	1.086
16	1.004
20	0.914
22	0.858
23	0.802

The optimal horizontal tail size was found to be 23 m² (247.57 ft²), due to it having the lowest moment coefficient along the pitch axis during flight. Based on the sized horizontal tail and vertical tail, a final static margin was also calculated, to make sure that the horizontal tail sizing process did not affect the static margin in a negative manner. This static margin was found to be 0.1926481681, which was within acceptable bounds.

9.2 Stability Analysis

Ensuring exact stability conditions was another important factor of consideration for the aerodynamics team. Accurate stability conditions were of the utmost importance as they would ensure the aircraft reached the aerodynamic benchmark for all of our design priorities. Stability is essential for ensuring the safety of passengers and crew. A stable aircraft is less likely to experience unexpected and potentially dangerous changes in flight attitude or behavior. A stable aircraft also provides a smoother and more comfortable ride for passengers, a major facet of any commercial aircraft. Finally, a stable aircraft is also important for maintaining fuel efficiency and reducing operating costs. A stable aircraft will require less corrective action from the pilot, which means less fuel will be consumed. The aircraft is stable in pitch because the center of gravity is located in front of the neutral point. The change of rolling moment coefficient with respect to sideslip angle represents the static lateral stability derivative. This value must be negative for the aircraft to have lateral static stability. It is the sum of the lateral stability derivatives for the wing, fuselage, and wing-fuselage components. For directional stability, the stability derivative must be greater than zero to ensure restoring moments will be generated to counteract sideslip correctly.

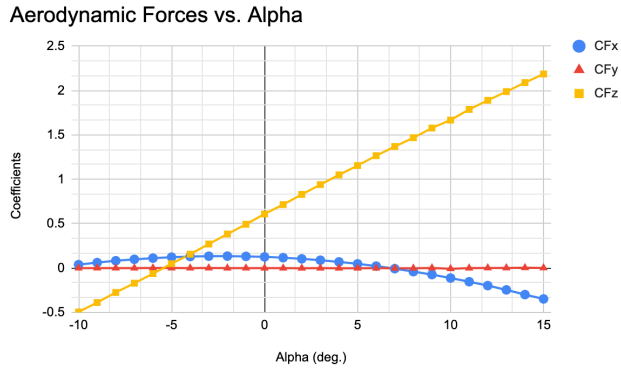


Figure 9.1: Aerodynamic Forces vs Angle of Attack at Takeoff

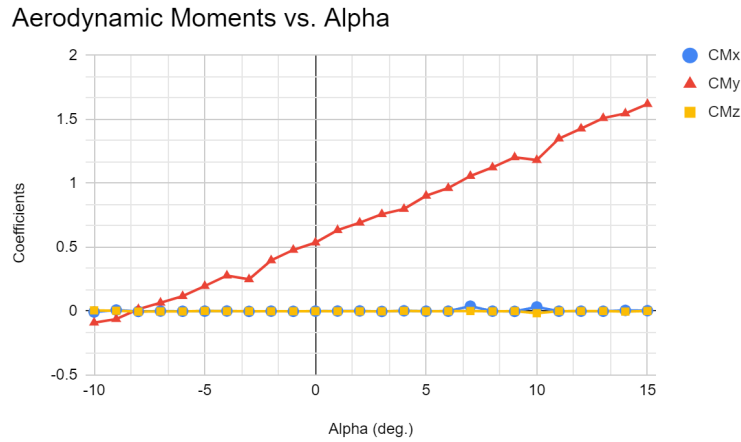


Figure 9.2: Aerodynamic Moments vs Angle of Attack at Takeoff

Table 9.3: Aircraft stability coefficients

Stability Coefficient	Value
CFx	0.16
CFy	-0.001
CFz	0.49
CMx	0.001
CMy	0.2
CMz	-0.002

CMI	-0.001
CMm	0.20
CMn	0.002

Force and moment stability coefficients were also calculated for the empennage with a sized vertical tail. In general, they were found to be within acceptable limits.

9.4 OEI Considerations

Wingtip-mounted propulsors present a unique challenge to managing OEI conditions. The thrust required to continue flight and maintain control combines with the drag from the feathered propellers on the inoperative engine to produce a yawing moment significantly greater than in a traditional configuration. To ensure Low Rider can maintain directional control, the size of VT and rudder must be sufficient to produce a counteracting moment. This was verified by calculating the required C_L of the VT to provide the force required.

FAR Part 25 defines maximum climb gradient required for a two-engined aircraft under OEI as 2.4%, achieved on climbout. This is the most extreme climb gradient required, and thus the point under OEI where the operative engine must produce the most thrust. For a climbout speed of approximately 130 kts, this equates to a rate of climb of approximately 273 ft/min. In order to overcome drag and provide sufficient excess power for climb, the operative engine must produce 4000 lbs of thrust, or approximately half of its rated thrust. In order to counteract the combined moment of this thrust and the inoperative engine's drag, the VT must achieve a C_L of at least 0.2.

Flightstream estimates that with a fully deflected rudder flying at 130 kts and sea-level, the VT's C_L is 1.25, or more than six times the required C_L to maintain directional control. The empennage is significantly larger than required to control the aircraft under OEI, and its sizing is thus dominated by stability requirements.

10. Performance Analysis

Performance analysis was an integral part of the entire design process, informing every major decision as the model was iterated. This was performed using FLOPS, with the goal of capturing as many metrics of interest as possible. Once Low Rider's design was complete, the finalized FLOPS model was run to evaluate its performance.

10.1 Block Fuel Burn and Emissions

As the primary metric of performance and driver of our first design priority, Low Rider’s design was focused on reducing block fuel burn relative to the baseline ATR 42-600 model developed. Block fuel was calculated on 200, 300, and 400 nm missions in addition to the 500 nm economic mission to capture Low Rider’s performance over a range of typical RT missions.

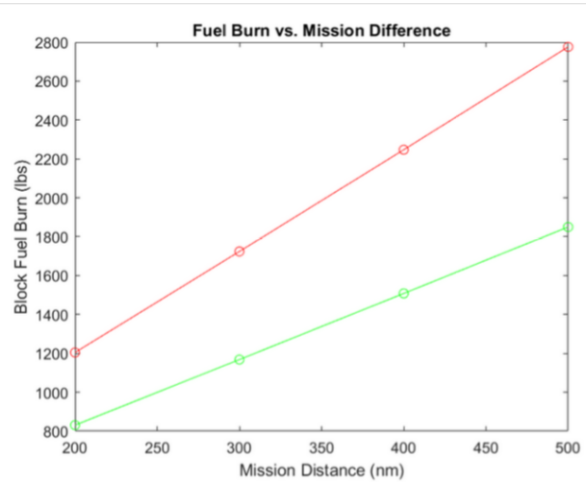


Figure 10.1: Economic Mission Block Fuel Burn Reductions Relative to ATR 42-600

With a projected 33.4% reduction in block fuel on the 500 nm economic mission, Low Rider realizes significant fuel savings. In order to determine the impact of this fuel burn reduction on overall emissions, CO₂ equivalent emissions were assumed to be 3.8 lbs for every pound of fuel burned, and 0.9 lbs for every kWh of energy used to charge the battery [40]. NO_x emissions were calculated using FLOPS estimates from the engine data.

Table 10.1: Summary of Block Fuel Burn and Emissions Reductions

	ATR 42-600	Low Rider	% Reduction
Block Fuel Burn (lbs)	2,776.1	1,850.1	33.4
NO _x Emissions (lbs)	22.7	22.5	0.9
CO ₂ Equivalent Emissions (lbs)	10,445.1	7,032.0	32.7

In order to characterize the benefits of various technologies applied, four aircraft models were developed:

- 1) ATR 42-600: This was the baseline model used to evaluate Low Rider’s performance against the design priorities

- 2) Next-Gen ATR 42: The baseline ATR 42-600, but equipped with a powerplant representative of technology available in 2034.
- 3) Advanced Baseline: A Low Rider without hybridization. Applies reductions in weight due to new technologies and materials expected to be available in 2035, such as wingtip propellers and PRSEUS
- 4) Low Rider: The final, fully-developed design with a hybrid-electric propulsion architecture

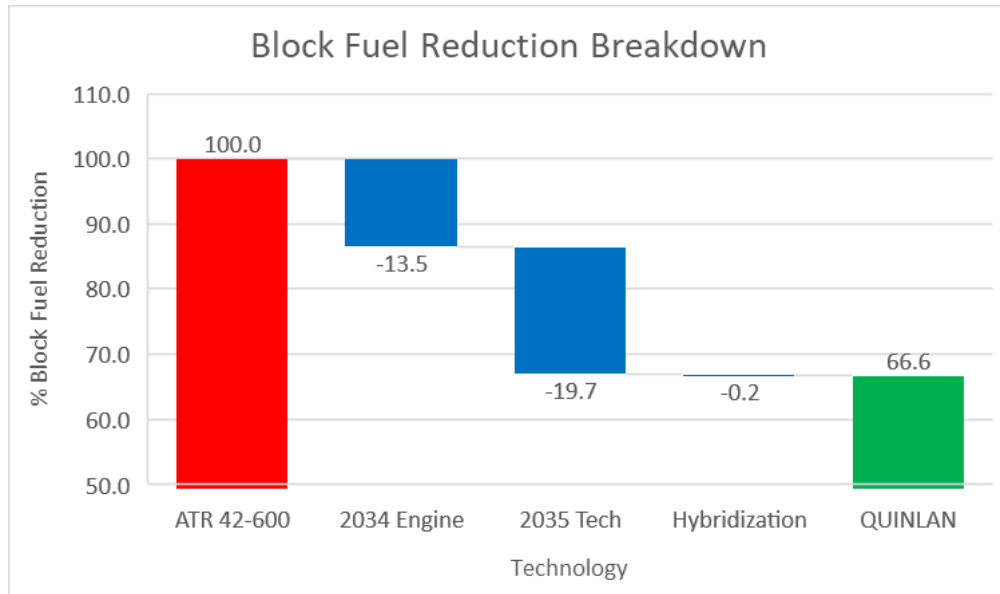


Figure 10.2: Share of Block Fuel Reduction Relative to the ATR 42-600 for Projected New Technologies

While hybridization does provide a small benefit to overall fuel consumption, Figure 10.2 shows that the vast majority of Low Rider’s block fuel reduction comes from advanced technologies. This is likely due to its relatively close EIS. Given more time, new technologies will be developed that can further decrease block fuel consumption. Regardless, Low Rider will reduce overall emissions, with the added benefit of operational cost savings that are passed down to the consumer through cheaper ticket prices.

10.2 Flight Envelope

The flight envelopes were determined using the method outlined in Roskam Volume V and in accordance with FAR Part 25 guidelines [41]. The maneuvering envelope defines the safe loads and speeds at which the aircraft can operate and maneuver, and the gust envelope defines the safe conditions where the aircraft can operate in gusty conditions. Using the Roskam method, it was determined that the key speeds for the Low Rider are as follows

Table 10.2: Key Aircraft Speeds

Key Speed	Definition	Value (KEAS)
V_{S1}	+1g Stall Speed	98.2
V_C	Design Cruise Speed	237.6
V_D	Design Diving Speed/Never Exceed Speed	297.0
V_A	Design Maneuvering Speed	158.5
V_B	Maximum Gust Intensity Speed	194.56

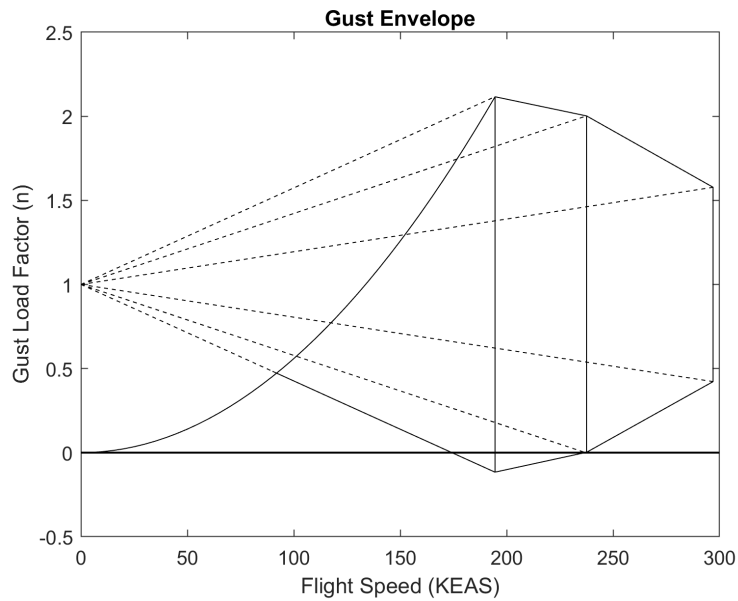


Figure 10.3: Gust Envelope

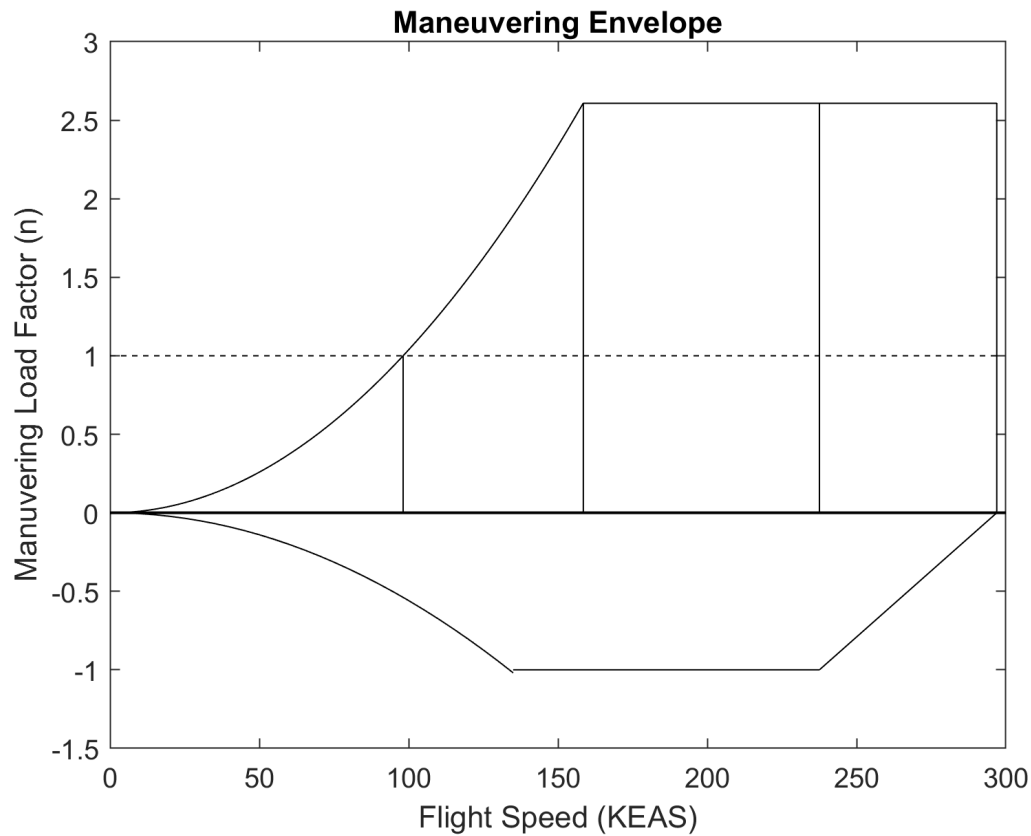


Figure 10.4: Maneuvering Envelope

10.3 Performance Summary

FLOPS was used to estimate the primary metrics of performance and calculate the relation between payload and range. Field lengths were calculated for the maximum takeoff and landing weights, while pounds of fuel burned per seat-mile and mission time were calculated for the economic mission. FLOPS estimates were considered to be reliable for every metric except landing field length, which was instead determined using the methods outlined in Nicolai and Carichner Chapter 5 [23]. A summary of Low Rider's performance can be found in Figure 10.5 and Table 10.3.

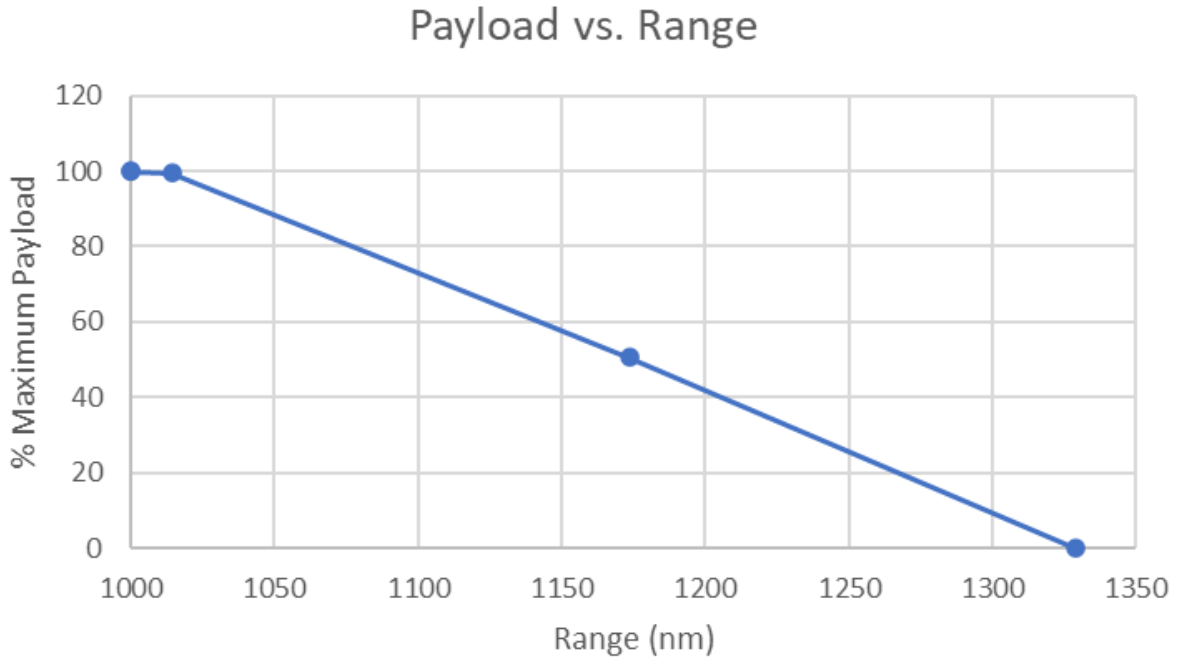


Figure 10.5: Payload-Range Diagram for Low Rider

Low Rider was designed to carry passengers on a maximum design mission of 1000 nm. Additional fuel savings or longer ranges are possible by reducing the number of passengers onboard. However, small fuel tanks result in a limited zero-payload ferry range of only 1329 nmi.

Table 10.3: Summary of Key Performance Metrics Relative to the ATR 42-600

Performance Metric	ATR 42-600	QUINLAN
lbs/seat-mile on 500 nm mission	0.116	0.077
Takeoff Field Length (ft) MSL / 5000 ft MSL	3,632 / 4,112	2,870 / 3,249
Landing Field Length (ft) MSL / 5000 ft MSL	3,196 / 3,477	2,608 / 2,834
OEW (lbs)	25,904	20,961
MTOW (lbs)	41,005	37,255
Economic Mission Time (min)	135	142
Maximum Range (nm)	726	1000

The short field variant of the ATR 42-600, the ATR 42-600S, is advertised to be capable of performing a 200 nm mission with a takeoff field length of only 2625 ft [42]. For the same 200 nm mission, FLOPS calculates Low Rider requires only 2602 ft of runway. By practically every metric, Low Rider outperforms the ATR 42-600. Shorter field lengths at all altitudes ensure it can access more airports in remote regions, and by burning lbs/seat-mile it can keep costs for both passengers and the airline low. A slightly slower cruise speed means that Low Rider takes 7 more minutes to complete the same economic mission, however this is almost negligible, especially once lower traveling costs are factored in. Additionally, this time difference will be far smaller on shorter flights, which are more representative of the typical missions Low Rider will perform.

11. Systems

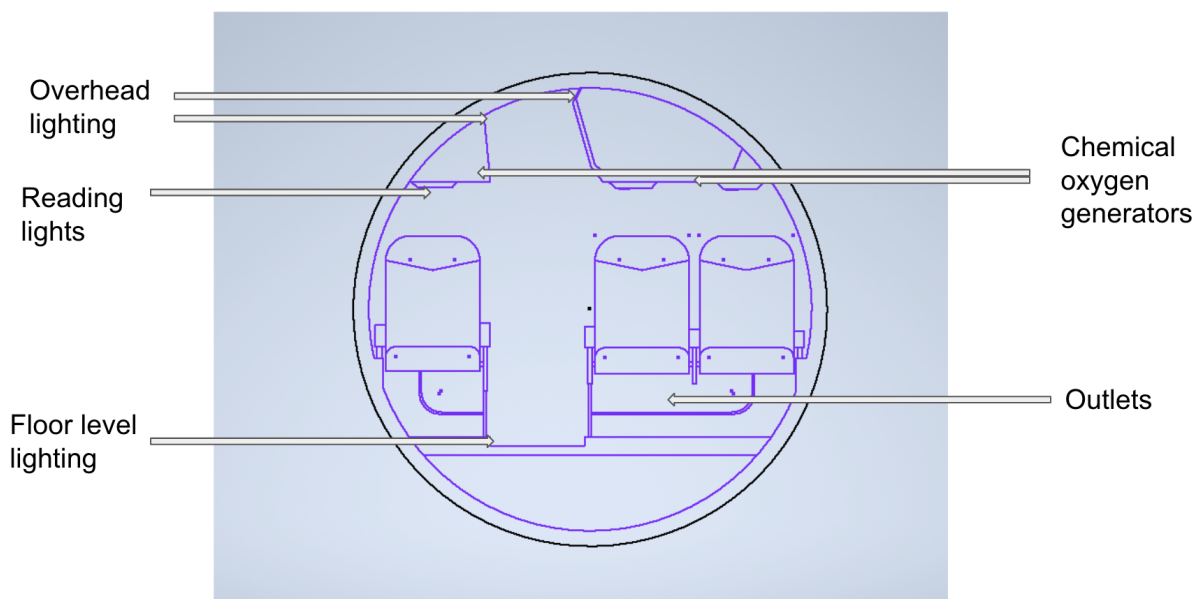


Figure 11.1: Interior Subsystems

11.1 Actively Tuned Vibration Absorbers (ATVAs)

In order to improve customer comfort and acceptance, several noise suppression techniques were considered. Active noise cancellation (ANC), while common in headphones, is difficult to control across an entire passenger cabin, as noise levels vary spatially. Even a small phase difference in the ANC can amplify noise

experienced by passengers [43]. The primary source of cabin noise in RTs is through structural vibrations. By targeting these vibrations, noise levels can be mitigated. Tuned vibration absorbers (TVAs) use tuned mass dampers to dampen or cancel out specific vibrations in the structure. A weakness of this approach is that the frequency range is fixed, and Low Rider will experience a range of frequencies as throttle setting and flight conditions change. Actively-tuned vibration absorbers (ATVAs) solve this problem by actively tuning the mass dampers using actuators [25], as seen in Figure 11.1 below.

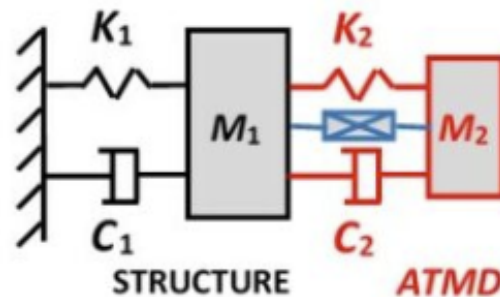


Figure 11.2: Configuration of ATVA Attached to Fuselage Structure [25]

Multiple ATVAs are fitted to the fuselage frame in order to reduce the severity of mechanical vibrations the cabin is subjected to. A computer combines ambient noise data from microphones in the cabin with engine RPM data to automatically adjust the frequency of noise dampers to cancel out these vibrations. This technology was initially introduced on the Dash 8 Q-series aircraft to great success [44], and will greatly improve cabin comfort.

11.2 Air Conditioning and Emergency Oxygen

Air conditioning and oxygen will be recirculated from air in the cabin using HEPA air filters. Pressurization will be required in flight, and the extra air for pressurization will be provided by the bleed air from the turbines. Emergency oxygen will be provided by chemical oxygen generators above each seat in the cabin. The generators and oxygen masks will be controlled by a pressure switch – if the pressure threshold is met, the generators will begin producing oxygen and the masks will be deployed from their compartments above the passengers.

11.3 Anti-Icing

Bleed air will be used to provide anti-icing capability to the aircraft. It was selected due to its simplicity, effectiveness, and commonality with other regional aircraft. A system of tubes near the leading edge of the wing will carry hot bleed air, raising the temperature of the leading edge. When water contacts the wing, it will evaporate, eliminating the chance of icing occurring on the aircraft. The system requires no additional energy aside from the bleed air, and does not rely on external power sources or electronics. Additionally, most turbine powered aircraft use this system, which will make maintenance familiar and easier for maintenance personnel who are used to working on turbine engined aircraft [45].

However, runback icing is still a problem with this system, as the bleed air will not reach areas of the wing not on the leading edge. Runback icing occurs when the bleed air is not hot enough to evaporate the ice, only melt it. This occurs when the engine is operating in low-power phases of flight, such as landing or holding. Additionally, once runback icing occurs, there is no way to solve the problem other than to land the aircraft and de-ice on the ground[46]. Therefore, for customers operating the Low Rider. in low-temperature austere environments, a supercooled large drop (SLD) guard will be offered. This consists of a thin titanium strip mounted on the upper and lower surfaces of the wings behind the leading edge. When turned on, these strips will weep a glycol solution that will prevent runback ice from forming by lowering the freezing temperature of the supercooled drops. As a result, aircraft equipped with this option will have the ability to operate in flight into known icing (FIKI) conditions for 45 minutes [47].

11.4 Fire Suppression

Fire suppression will be split into three distinct systems. For fires in the passenger cabin and cockpit, handheld halon canisters will be available for use by the flight crew [48]. For fires in the engine, fire bottles will be placed in the engines and can be remotely deployed from the flight deck. Lastly, the cargo hold will have an automatic fire suppression system engaged by smoke detectors [49].

11.5 Fly-By-Light / Power-By-Wire (FBL/PBW)

The unique propeller location of the Low Rider. requires significant yaw correction under OEI conditions. In a traditional mechanical control system, the pilot would have to apply manual force on the controls in order to maintain directional control. This would exhaust the pilot and reduce situational awareness, increasing the risk of an accident.

By translating pilot inputs into digital signals sent to electronic actuators on the control surfaces, an FBL system requires far less mental and physical effort to control the aircraft. In case of an engine failure, a switch can be activated that would automatically correct for the drastically increased yaw. Although almost identical in operating principle to fly-by-wire, FBL uses fiber optics in place of traditional wires to transmit control signals. This translates to higher signal bandwidth, lighter system weight, and significantly reduced risk of electromagnetic interference. Power is provided to control surface actuators by wiring. The elimination of a distributed hydraulic system and the use of triple-redundant control actuators significantly improves reliability and maintainability. Gains in engine efficiency are also realized, as the need for bleed air to power hydraulic systems is reduced [50].

Compared to a conventional mechanical control system, FBL can be over 2000 lbs lighter on a commercial widebody aircraft [ieee]. According to FLOPS estimates, the hydraulic system weight accounts for approximately 1% of the empty weight of aircraft. Lacking any readily available sources on FBL integration into RT aircraft, the Boeing 747, a common widebody at the time of the paper's publication (1993), was instead used to develop relationships for weight savings. The empty weight of a 747 is approximately 412,000 lbs, thus it was assumed that the mechanical flight control system weighs 4120 lbs [51]. A 2000 lb weight reduction would equate to an FBL system weighing only 49% of the hydraulic system. Applying this relationship to our aircraft yields a weight reduction of 151 lbs.

With documented use of FBL in both military and civilian aircraft, such as the Kawasaki P-1 [52], this is a viable option for Low Rider. Significant weight savings, combined with the increased reliability, redundancy, and maintainability of the FBL system justify its application on the Low Rider. despite its increased up-front cost and electrical power draw.

11.6 Full-Authority Digital Engine Control (FADEC)

The Low Rider uses a double-redundant FADEC system to control the engine's throttle setting, fuel mixture, and propeller pitch automatically through throttle input and continuous digital signals to the engine. This system ensures that the powerplant is always operating at its ideal point, increasing efficiency and therefore fuel economy. Pilot workload in critical phases of flight is reduced by simplifying the engine controls from six levers to only two. FADEC prevents pilots from accidentally running the engine beyond its continuous operational limits, however manual override is available to permit over-running the engine in emergency situations. Combined with increased engine monitoring capabilities, redundancy, and greater reliability, FADEC allows for far safer, more efficient aircraft operation. [53]

11.7 Non-Propulsive Electrical System

Electrical power is provided to the cabin and cockpit through a battery separate from the propulsion system battery. This increases redundancy and simplifies the wiring and discharge modulation required for each battery. The battery is charged either by an external power unit connected via wire, when the engines are shut down, or by using the HEMM as a generator when the engines are running. The non-propulsion battery is slightly upsized to ensure sufficient energy is stored for the takeoff and climb segment, when the HEMM is being used as a motor.

In order to minimize weight and simplify the aircraft, Low Rider does not have an APU. When power is required on the ground and there is no access to an external power source, the starboard engine includes a "propeller brake," allowing it to run in "hotel mode," using the turbine to run the HEMM as a generator without turning the propeller and producing thrust. ATR aircraft use this system [54], and although louder and less efficient on the ground, approximately 300 lbs of weight were saved according to FLOPS estimates. This gain in performance and reduction in cost by using a propeller brake was considered sufficient to outweigh its drawbacks.

12. Interior Layout

12.1 Fuselage Configuration

Fuselage configuration and shape is driven by the passenger cabin. In order to determine the optimal cabin layout, appropriately sized FLOPS models were developed for 46, 48, and 50 passengers in both a 2-2 and 2-1 seating configuration. The performance of these models was then evaluated on the 500 nm economic mission with the goal of minimizing aircraft cost. The two drivers of aircraft cost were assumed to be acquisition cost (assumed to scale with OWE) and operating cost (assumed to scale with lbs of fuel burn per seat-mile). In order to capture and evaluate the total relative costs, a cost metric was developed by multiplying lbs/seat-mile with OWE.

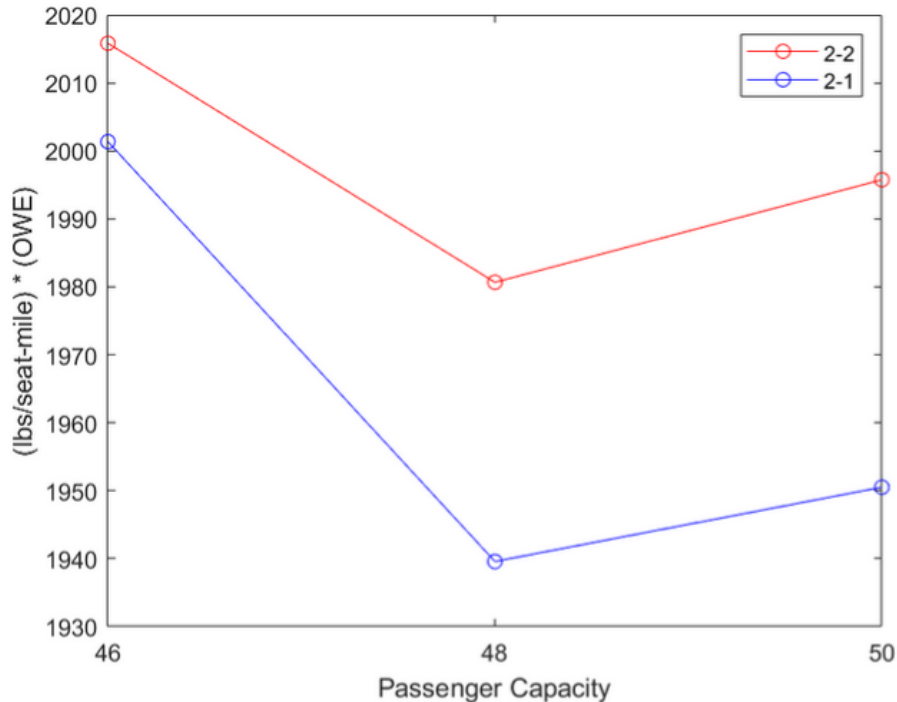


Figure 12.1: Fuel Burn per Seat-Mile • Operating Weight Empty vs Passenger Capacity

Due to improved aerodynamics and a reduced empennage size via increased moment, the cost metric was significantly lower in the 2-1 configuration, with a minimum point at 48 passengers. An additional benefit of 48 passengers is that 48 is evenly divisible by three seats. This reduces extra space, and thus fuselage length, which

would be required by including an extra incomplete row. This justifies Low Rider's cabin configuration of 48 passengers in a 2-1 configuration.

12.2 Passenger Cabin

The aircraft is designed to accommodate 48 passengers each weighing 200 lbs and carrying 40 lbs (5 ft³) of baggage. Each seat has a width of 18 inches with 2 inch arm rests on either side. The aisle width will be at least 18 inches. The aisle height will be comparable to standard regional turboprop aircraft. The seats will have reclining capabilities and have foot space and storage comparable to similar aircraft. The baggage compartment in the aisle will be tall enough to be serviced ergonomically for a majority of passenger heights. The top down, side view, and cross section views of the aircraft can be seen below. A few other key features include the galley located at the front left of the cabin, bathroom located at front left, and the rear luggage compartment. The aircraft will be equipped with Wi-Fi and a USB outlet for every passenger. Each seat will have a reading light and there will be lights above the passenger cargo compartments. Floor level lighting will illuminate in the case of an emergency. Cabin power will be provided by a separate battery, charged by using the HEMM as a generator.

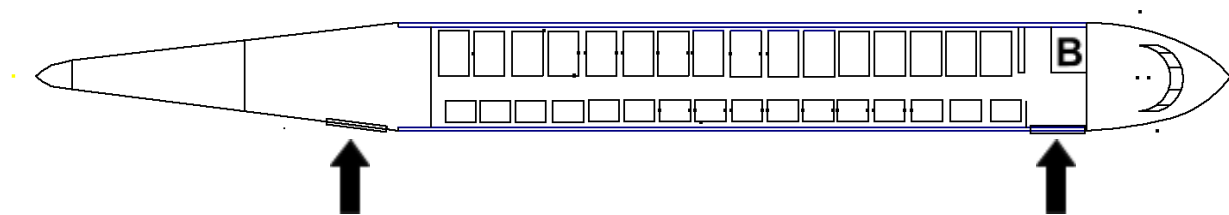


Figure 12.2: Top-Down View of Cabin Layout. Location of Passenger Entrance Indicated by the Black Arrow

EMERGENCY EXIT LOCATIONS

THESE WILL MEET DITCHING REQUIREMENTS

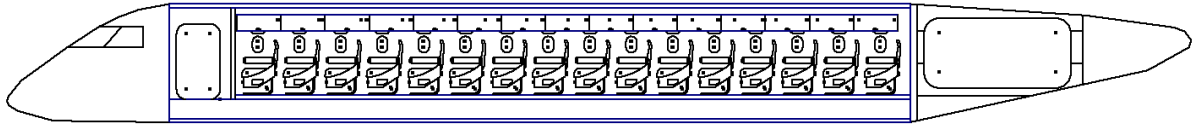


Figure 12.3: Fuselage Centerline Diagram

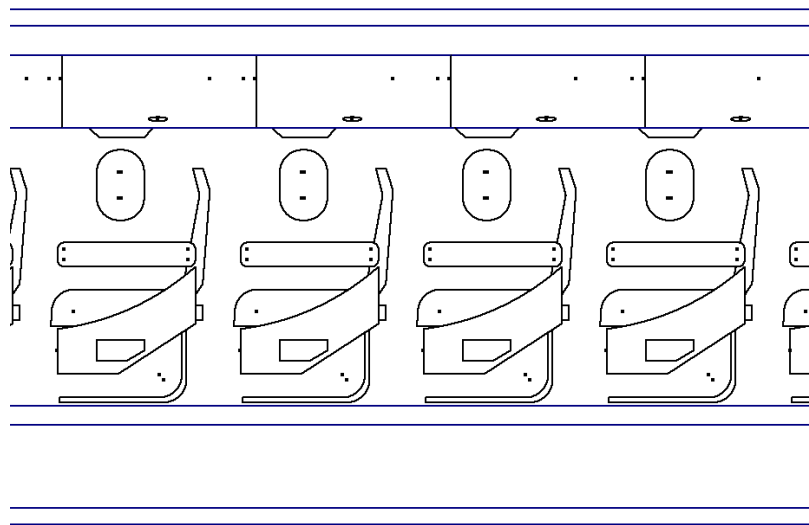


Figure 12.4: Closeup View of Seats

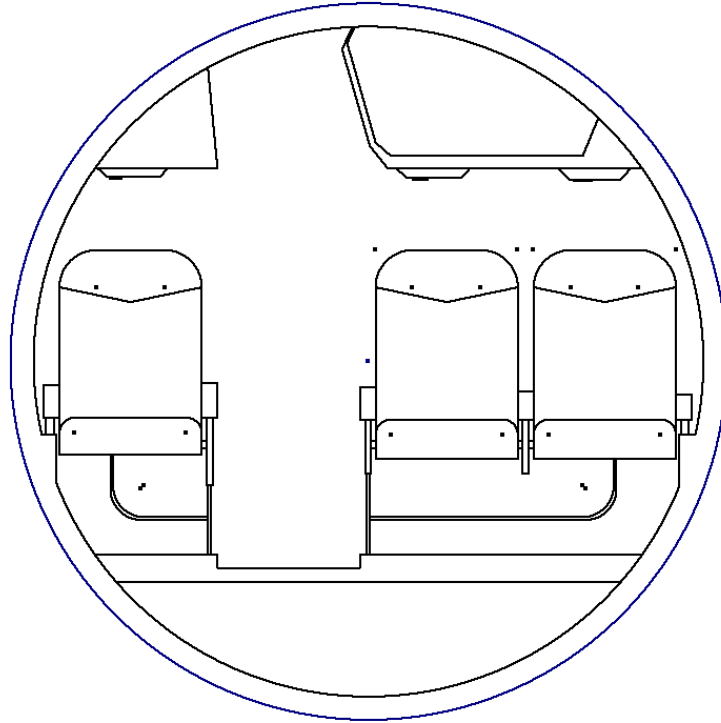


Figure 12.5: Cross-Section of Fuselage

Several state of the art weight reducing technologies were used when designing the Low Rider. The first of which is the use of the Expliseat for passenger seating. The Expliseat TISEAT E2 S-Line weighs in at just 12.8 lbs per passenger, representing a 40% weight reduction compared to conventional passenger seats [55]. Another cabin weight reduction applied is the use of polycarbonate (PC) sheet for interior finishings. The use of PC can represent a weight savings of 40% compared to standard polyvinyl chloride and acrylic blend (PMMA/PVC) sheets. Based on a 48 seat aircraft, this would result in a 67.7 lb weight reduction. Additionally, due to PMMA/PVC's high toxicity, using PC for interior finishing has the added benefit of a safer manufacturing process [56]. In total, these weight reductions result in a 477.3 lb weight reduction for the Low Rider's cabin.

12.3 Cockpit

Low Rider. is equipped for both VFR and IFR flight per FAR Part 25. The nose is angled to be flush with the windshield in order to provide maximum visibility on steep approaches, which may be encountered in mountainous terrain. Although FBL allows for the possibility of a sidestick, the cockpit is kept similar in layout and

control scheme to existing competitors such as on the Saab 2000, as seen in Figure 12.6. This will make it easier for pilots to re-train and transition to this aircraft, and require fewer adjustments to new pilot training programs. A similar cockpit also means fewer new pieces of equipment need to be designed.



Figure 12.6: Interior of Saab 2000 Cockpit

12.3.1 Avionics

A full “glass cockpit” enables far greater flexibility in cockpit design and capabilities. LCDs are cheaper, lighter, and more reliable than traditional avionics, and the avionics software can be easily updated in very little time. This will keep costs down by reducing the number of new components and instruments that need to be designed, and the maintenance and additional training of maintenance personnel required. The primary flight display includes a synthetic vision system (SVS), using a 3D representation of the environment generated from GPS and IMU data to increase pilot situational awareness. To further increase safety in low-visibility conditions, an enhanced flight vision system (EFV) is available on the flip-down HUD to complement the SVS. The EFV draws information from a nose-mounted infrared camera, which then projects the outside view onto the HUD (Figure 12.7). In addition to improved situational awareness, aircraft equipped with FAA-certified EFVSs are permitted to fly lower approaches in poor visibility. This improves the chances of spotting the runway, and thus of successfully landing, in adverse weather conditions [57].

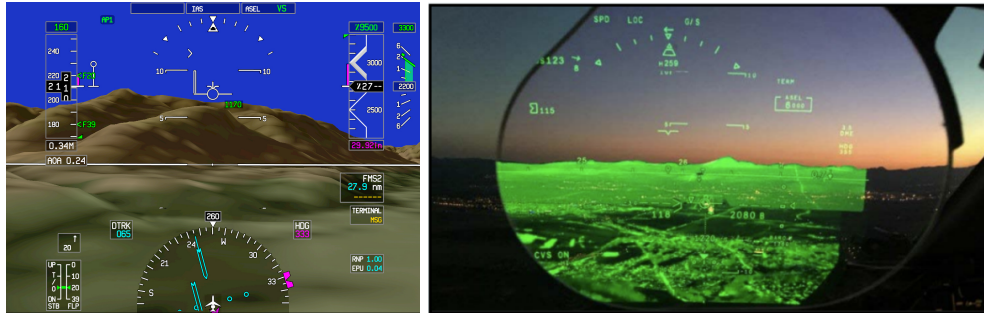


Figure 12.7: Examples of SVS (left) and EFVS (right) Displays

12.3.2 Autonomous Operation

The unpredictable nature of flight conditions in remote areas, reduced safety, and current near-term regulatory outlook make autonomous operations an unnecessary and expensive addition whose benefits could not be realized. A slightly more likely, and more regulatorily feasible, near-term possibility is single-pilot operations. With the advent of increased AI capabilities, it is conceivable that AI-driven pilot-assisting technologies could be implemented to the point where only one human operator would be required. Although neither of these capabilities were accounted for in Low Rider's design, the flexibility granted by electronic flight instruments, and the computerized link between flight controls and control surfaces via FBL, means that the appropriate software could be easily incorporated into the control system to enable either autonomous or single-pilot operations in the future.

13. Maintenance

The aircraft is designed with reliability as one of its top priorities. The maintenance requirements for the aircraft are very low. The aircraft will comply with general maintenance suggested by the FAA. Similarly, all standard maintenance can be expected to be the same as traditional regional turboprop aircraft. Any additional maintenance requirements set forth by the FAA for utilizing hybrid-electric aircraft will be complied with. The key difference in this aircraft from traditional aircraft is the addition of battery equipment. The battery will be located at a central location below the fuselage. This is to ensure the battery pack is located a considerable distance away from the fuel tanks. The battery can be recharged with the electric recharging port located at the bottom of the fuselage. Additionally, the batteries below the fuselage can be accessed via the entrance panel at the bottom of the fuselage.

There are a few dangers to this location. In the event of a crash the battery pack may catch on fire. Additionally, emergency landing on water may cause electrical danger. However, there are many benefits to the battery pack's location. The battery pack and recharge port are located a considerable distance away from each other to ensure no flame hazards occur during recharging. Similarly in the case of sparks or an explosion, which is quite low, the battery pack will not interact with the fuel tanks.

14. Cost Estimation

The final costing model shows our aircraft presenting a higher initial purchase price, but with lower operating and lifecycle costs. The following table shows costing alongside the ATR 42-600, which was used as a comparator aircraft [58][59].

Table 14.1: Costing Summary

Cost per Aircraft	ATR 42-600	Low Rider
Market Price	\$9.5 million	\$19.9 million
Lifetime Operating Cost	\$337.674 million	\$286.9 million
Hourly Operating Cost	\$7,656.25	\$8,533.25
Life Cycle Cost	\$359.43 million	\$307.3 million

In addition to a cost comparison, a comparative study was done to estimate the breakeven point of fuel vs battery and recharging costs overtime. The results, present in Figure 14.1, show that savings on fuel costs begin after the 60th mission, with a total fuel savings of \$7.3 million over the life cycle of the aircraft (estimated to be 30 years). The difference in costs includes an increased initial cost of the battery and regular replacement as well as the lower cost of refueling our hybrid aircraft.

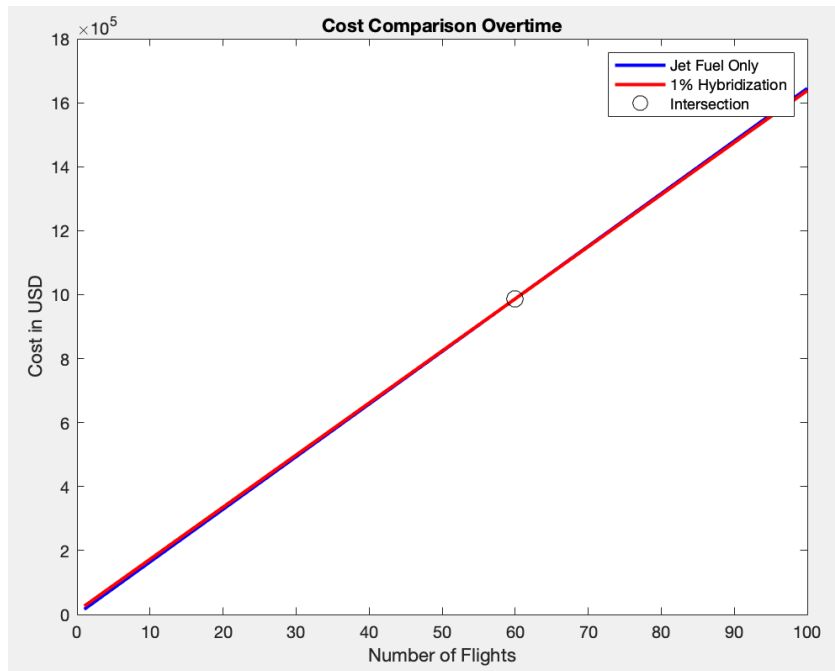


Figure 14.1: Refueling Cost Comparison

15. Conclusion

Low Rider's unique application of advanced technologies will help lead aviation towards a greener future. With 33% lower block fuel burn and emissions on an economic mission and strong short-field performance, this modern, comfortable aircraft exceeds the performance of current competitors by practically every metric. Mild hybridization, reliability, and ease of maintenance will keep operational costs low, making Low Rider an easy choice for forward-thinking regional airlines. Built from the ground-up with adverse weather conditions and traditionally inaccessible areas in mind, Low Rider will play an integral role in more sustainably connecting the world.

References

- [1] Marien, T. V., Antcliff, K. R., Guynn, M. D., Wells, D. P., Schneider, S. J., Tong, M., Trani, A. A., Hinze, N. K., & Dollyhigh, S. M. (2018, May). Short-haul revitalization study final report - NASA technical reports server (NTRS). NASA. <https://ntrs.nasa.gov/citations/20180004393>
- [2] *Turboprop market forecast 2022-2041*. ATR. (2022, September 30). <https://www.atr-aircraft.com/our-aircraft/turboprop-market-forecast-2022-2041/>
- [3] ATR. (n.d.). *ATR 42-600*. ATR. https://www.atr-aircraft.com/wp-content/uploads/2022/06/ATR_Fiche42-600-3.pdf
- [4] ATR - Official Website - Air Tahiti. Official website. (n.d.). <https://www.airtahiti.com/en/atr>
- [5] ATR 42-600 - price, Specs, photo gallery, history. Aero Corner. (n.d.). <https://aerocorner.com/aircraft/atr-42-600/>
- [6] Bonnassies, O. (2019, December 6). *Bombardier to discontinue Q200/Q300 in 2009*. Flight Global. <https://www.flightglobal.com/bombardier-to-discontinue-q200/q300-in-2009/79686.article>
- [7] Bombardier Q300 - price, Specs, photo gallery, history. Aero Corner. (n.d.-b). <https://aerocorner.com/aircraft/bombardier-q300/>
- [8] SomeRando, & Victor. (2020, January 25). *Home*. commercial aircraft. Pictures, specifications, reviews. <https://www.airlines-inform.com/commercial-aircraft/dash-8q300.html>
- [9] *Saab 2000: Saab*. Start. (n.d.). <https://www.saab.com/products/saab2000>
- [10] Planespotters.net. (n.d.). <https://www.planespotters.net/production-list/Saab/2000?sort=status>
- [11] Finlay, M. (2022, March 26). 30 years of Flight: The story of the Saab 2000. Simple Flying. https://simpleflying.com/saab-2000-30-years-story/?newsletter_popup=1
- [12] *Saab 2000 private jet charter, hire costs, and rental rates*. Paramount Business Jets. (n.d.). <https://www.paramountbusinessjets.com/private-jet-charter/aircraft/saab-2000>
- [13] *Saab 2000 - price, Specs, photo gallery, history*. Aero Corner. (n.d.-c). <https://aerocorner.com/aircraft/saab-2000/>
- [14] *ERJ145*. Embraer. (2021, September 23). <https://www.embraercommercialaviation.com/commercial-jets/erj145/>
- [15] Nowack, T. (2020, July 6). Embraer delivers very last ERJ. aeroTELEGRAPH. <https://www.aerotelegraph.com/en/end-production-embraers-last-erj-has-been-delivered-to-germany>
- [16] RZjets.net. (n.d.). Embraer ERJ-135 600/650, Embraer ERJ-145 production list. <https://rzjets.net/aircraft/?typeid=111>
- [17] *Embraer ERJ 145 - price, Specs, photo gallery, history*. Aero Corner. (n.d.-c). <https://aerocorner.com/aircraft/embraer-erj-145/>
- [18] *Scholarly Commons: Embry-Riddle Aeronautical University Research*. Site. (n.d.). <https://commons.erau.edu/>
- [19] Images, Z. S. (2019, February 4). I'm flying in that? unloved turboprop gets second look. The Wall Street Journal. <https://www.wsj.com/articles/im-flying-in-that-unloved-turboprop-gets-second-look-11549277255>
- [20] NASA. (2016, November 8). Flight Optimization System Release 9.0.0 User's Guide.
- [21] ES-30. Heart Aerospace. (n.d.). <https://heartaerospace.com/es-30/>
- [22] The Federal Register. Federal Register :: Request Access. (n.d.). <https://www.ecfr.gov/current/title-14/chapter-I/subchapter-C/part-25?toc=1>
- [23] Carichner, G. E., & Nicolai, L. M. (2013). *Fundamentals of aircraft and Airship Design*. American Institute of aeronautics and astronautics.
- [24] Antcliff, K. R., and Capristan, F. M., "Conceptual design of the parallel electric-gas architecture with Synergistic Utilization Scheme (Pegasus) concept," 18th AIAA/ISSMO Multidisciplinary Analysis and Optimization Conference, 2017.

- [25] Wright, R. I., & Kidner, M. R. F. (2004, August). Sage Journals. <https://journals.sagepub.com/doi/epdf/10.1177/1077546304041368>
- [26] Pastra, C., Cinar, G., Mavris, D. (2022). Feasibility and benefit assessments of hybrid hydrogen fuel cell and battery configurations on a regional turboprop aircraft. *AIAA Aviation 2022 Forum*.
<https://doi.org/10.2514/6.2022-3290>.
- [27] Antcliff, K., Guynn, M., Marien, T., Wells, D., Schneider, S., & Tong, M. (2016). Mission Analysis and Aircraft Sizing of a Hybrid-Electric Regional Aircraft. 54th AIAA Aerospace Sciences Meeting.
<https://doi.org/10.2514/6.2016-1028>.
- [28] Kyprianidis, K. (2011). Future Aero Engine Designs: An Evolving Vision. *Advances in Gas Turbine Technology*. Intech. <https://www.intechopen.com/chapters/22893>.
- [29] Schnulo, S. L., Chapman, J. W., Hanlon, P., Hasseeb, H., Jansen, R., Sadey, D., Sozer, E., Jensen, J., Maldonado, D., Bhamidapati, K., Heersema, N., Antcliff, K., Frederick, Z. J., & Kirk, J. (2020). Assessment of the impact of an advanced power system on a Turboelectric single-aisle concept aircraft. *AIAA Propulsion and Energy 2020 Forum*. <https://doi.org/10.2514/6.2020-3548>.
- [30] Colozza, A. (2002). Hydrogen Storage for Aircraft Applications Overview. NASA Glenn Research Center Report. <https://ntrs.nasa.gov/api/citations/20020085127/downloads/20020085127.pdf>.
- [31] The Tesla Team. (2019, March 6). Introducing V3 supercharging. Tesla.
<https://www.tesla.com/blog/introducing-v3-supercharging>.
- [32] Kellermann, H., Fuhrmann, S., & Hornung, M. (2021). Design of a battery cooling system for hybrid electric aircraft. *AIAA AVIATION 2021 FORUM*. <https://doi.org/10.2514/6.2021-3138>
- [33] Culley, D., Kratz, J., Thomas, G. (2018). Turbine Electrified Energy Management (TEEM) For Enabling More Efficient Engine Designs. *2018 Joint Propulsion Conference*. <https://doi.org/10.2514/6.2018-4798>.
- [34] PRSEUS acoustic panel fabrication - NASA technical reports server (NTRS). (n.d.).
<https://ntrs.nasa.gov/api/citations/20120002663/downloads/20120002663.pdf>
- [35] Aluminum 7075-T6; 7075-T651. (n.d.). <https://www.matweb.com/search/DataSheet.aspx?MatGUID=4f19a42be94546b686bbf43f79c51b7d>
- [36] Overview of materials for epoxy/carbon fiber composite. (n.d.). https://www.matweb.com/search/datasheet_print.aspx?matguid=39e40851fc164b6c9bda29d798bf3726
- [37] Niu, M. C. Y. (2016, July 4). Airframe structural design: Practical design information and data M. C. Y. Niu Second Edition. distributed by Adaso/Adastra Engineering Center, PO box 3552, Granada Hills, CA 91394, USA, 1999. 612PP. illustrated. \$65. ISBN 962-7128-09-0.: The Aeronautical Journal. Cambridge Core.
<https://www.cambridge.org/core/journals/aeronautical-journal/article/abs/airframe-structural-design-practical-design-information-and-data-m-c-y-niu-second-edition-distributed-by-adasoadastra-engineering-center-po-box-3552-granada-hills-ca-91394-usa-1999-612pp-illustrated-65-isbn-9627128090/0940456E5F10A10B25FFD8E7C6438B1B>
- [38] Aircraft fuel pumps 101. Quality Aircraft Accessories. (2023, April 13).
<https://www.qaa.com/aircraft-fuel-pumps#:~:text=Aircraft%20fuel%20pumps%20are%20an,proper%20pressure%20during%20engine%20operation>.
- [39] *ATR approved for unpaved runway operations in Russia's Siberia and Far East*. ATR. (n.d.-b).
<https://www.atr-aircraft.com/presspost/atr-approved-for-unpaved-runway-operations-in-russias-siberia-and-far-east/>
- [40] Marien, T. V., Blaesser, N. J., Frederick, Z. J., Guynn, M. D., Fisher, K. L., Schneider, S. J., Thacker, R. P., & Frederic, P. (2021, August 2). *Methodology Used for an Electrified Aircraft Propulsion Design Exploration*. AIAA.
<https://arc.aiaa.org/doi/pdf/10.2514/6.2021-3191>
- [41] Roskam, J. (n.d.). *Airplane Design, part 3*. Google Books. https://books.google.com/books/about/Airplane_Design.html?id=_FBLtC3qpr4C

- [42] *ATR 42-600 STOL aircraft: ATR aircraft*. ATR. (2023, March 23). <https://www.atr-aircraft.com/our-aircraft/atr-42-600s-stol/>
- [43] Kaur, A. (2022). Tuned Absorbers/Dampers. *DEICON*. <https://deicon.com/solutions/tuned-absorbers-dampers/>
- [44] Global, F. (2019). Quiet revolution. *Flight Global*. <https://www.flightglobal.com/quiet-revolution/31793.article>
- [45] In-Flight Icing: Aircraft Design for Icing - Anti-Icing Systems. (n.d.). https://aircrafticing.grc.nasa.gov/1_1_3_6.html#:~:text=Anti%2Dicing%20systems%20are%20designed,to%20supply%20the%20required%20heat.
- [46] Contributors, T. S. &. (2021, April 26). Types of anti-icing systems in gas turbines. *Turbomachinery Magazine*. <https://www.turbomachinerymag.com/view/types-of-anti-icing-systems-in-gas-turbines>
- [47] *SLD - CAV Systems*. (2020, February 12). CAV Systems. <https://www.cav-systems.com/sld/>
- [48] AERO - Fire Protection: Cargo Compartments. (n.d.). https://www.boeing.com/commercial/aeromagazine/articles/2011_q2/3
- [49] Aircraft Fire Extinguishing Systems | SKYbrary Aviation Safety. (n.d.). <https://www.skybrary.aero/articles/aircraft-fire-extinguishing-systems>
- [50] Integrating fly-by-light/power-by-wire flight control systems on transport aircraft. (1993). IEEE Conference Publication | IEEE Xplore. <https://ieeexplore.ieee.org/stamp/stamp.jsp?tp=&arnumber=28350>
<https://global.kawasaki.com/en/corp/rd/magazine/179/pdf/n179en13.pdf>
- [51] FlightDeckFriend.com. (2023, February 10). How Much Does a Jumbo Jet Weigh | FlightDeckFriend.com. FlightDeckFriend.com | Pilot Jobs | Flight Training | Aspiring Pilots. <https://www.flightdeckfriend.com/ask-a-pilot/how-much-does-a-747-weigh#:~:text=The%20weight%20of%20an%20empty,91%2C300%20lb%20%2F%2041%2C413%20kg>
- [52] *New Product Introduction: Maritime Patrol Aircraft P-1 and Cargo Aircraft C-2*. (2018, November). [global.kawasaki.com](https://global.kawasaki.com/en/corp/rd/magazine/179/pdf/n179en13.pdf). Retrieved May 12, 2023, from <https://global.kawasaki.com/en/corp/rd/magazine/179/pdf/n179en13.pdf>
- [53] Federal Aviation Administration. (n.d.). Full Authority Digital Engine Control (FADEC).
- [54] Jakobi, S. (2021). The APU: The Hidden Engine. *Aviation for Aviators*. <https://aviationforaviators.com/2021/02/19/the-apu-the-hidden-engine/>
- [55] Seat lines - products - explisecat - comfort and Sustainability. Explisecat. (2021, October 19). <https://www.explisecat.com/products-seat-lines/>
- [56] 16, P. S. M. (2016, March 3). Durable, lightweight PC sheet homes in on aircraft interiors. [plasticstoday.com](https://www.plasticstoday.com/durable-lightweight-pc-sheet-homes-aircraft-interiors). <https://www.plasticstoday.com/durable-lightweight-pc-sheet-homes-aircraft-interiors>
- [57] Enhanced Vision Systems - Federal Aviation Administration. (n.d.-a). https://www.faa.gov/news/safety_briefing/2018/media/SE_Topic_18-01.pdf
- [58] ALLPIRG/4-WP/28 Appendix - International Civil Aviation Organization (ICAO). (n.d.-a). <https://www.icao.int/Meetings/AMC/MA/2001/Allpirg4/wp28app.pdf>
- [59] 19T0916 brochure booklet ATR family 105X200 V7. (n.d.-a). https://www.atr-aircraft.com/wp-content/uploads/2020/07/Factsheets_-_ATR_42-600.pdf
- [60] Preger, Y., Barkholtz, H. M., Fresquez, A., Campbell, D. L., Juba, B. W., Romàn-Kustas, J., Ferreira, S. R., & Chalamala, B. (2020). Degradation of commercial lithium-ion cells as a function of chemistry and cycling conditions. *Journal of The Electrochemical Society*, 167(12), 120532. <https://doi.org/10.1149/1945-7111/abae37>